Experimental, Numerical, and Analytical Slosh Dynamics of Water and Liquid Nitrogen in a Spherical Tank

by

Jedediah Morse Storey

A thesis submitted to the
Florida Institute of Technology
in partial fulfillment of the requirements
for the degree of

Masters of Science
in
Aerospace Engineering

Melbourne, Florida
May, 2016

We the undersigned committee hereby approve the attached thesis, "Experimental, Numerical, and Analytical Slosh Dynamics of Water and Liquid Nitrogen in a Spherical Tank," by Jedediah Morse Storey.

_____

Daniel Kirk, Ph.D.
Professor and Associate Dean
Department of Mechanical and Aerospace Engineering

_____

Ju Zhang, Ph.D.
Assistant Professor
Department of Mechanical and Aerospace Engineering

_____

Semen Koksal, Ph.D.
Professor
Department of Mathematics

_____

Hamid Hefazi, Ph.D.
Department Head
Department of Mechanical and Aerospace Engineering

Abstract

Title: Experimental, Numerical, and Analytical Slosh Dynamics of Water and Liquid Nitrogen in a Spherical Tank

Author: Jedediah Morse Storey

Advisor: Daniel Kirk, Ph. D.

Understanding, predicting, and controlling fluid slosh dynamics is critical to safety and improving performance of space missions when a significant percentage of the spacecraft's mass is a liquid. Computational fluid dynamics simulations can be used to predict the dynamics of slosh, but these programs require extensive validation. Many experimental and numerical studies of water slosh have been conducted. However, slosh data for cryogenic liquids is lacking. Water and cryogenic liquid nitrogen are used in various ground-based tests with a spherical tank to characterize damping, slosh mode frequencies, and slosh forces. A single ring baffle is installed in the tank for some of the tests. Analytical models for slosh modes, slosh forces, and baffle damping are constructed based on prior work. Select experiments are simulated using a commercial CFD software, and the numerical results are compared to the analytical and experimental results for the purposes of validation and methodology-improvement.

Table of Contents

List of Figures

List of Tables

List of Abbreviations

ASAP	-	Aerospace Systems and Propulsion laboratory
CFD	-	Computational Fluid Dynamics
CFM	-	Cryogenic Fluid Management
CMDLD	-	Center of Mass-Derived Logarithmic Decrement
CNC	-	Computer Numerical Control (machining)
CNES	-	Centre national d'études spatiales
COTS	-	Commercial Off The Shelf
DNS	-	Direct Numerical Simulation
DOF	-	Degree Of Freedom
ECLSS	-	Environmental Control and Life Support Systems
FDLD	-	Force-Derived Logarithmic Decrement
GRC	-	Glenn Research Center
ISS	-	International Space Station
KSC	-	Kennedy Space Center
LH_2	-	Liquid Hydrogen
LN_2	-	Liquid Nitrogen
LOx	-	Liquid Oxygen
LSP	-	Launch Services Program
MLI	-	Multi-Layer Insulation
MSFC	-	Marshall Space Flight Center
NSTRF	-	NASA Space Technology Research Fellowship
PCB	-	Printed Circuit Board
PLC	-	Programmable Logic Controller
STMD	-	Space Technology Mission Directorate
WH	-	Wall Height or Wave Height
WHDLD	-	Wall Height-Derived Logarithmic Decrement

Nomenclature

Bo	=	Bond number, $\Delta\rho g l^2/\sigma$
C_1A	=	baffle blockage area [m^2]
D	=	tank diameter [m]
D_n ,E_n	=	coefficients for slosh force calculations
f_d	=	wave amplitude depth function for baffles
F_S	=	slosh forces [N]
g	=	gravitational constant [m/s^2]
h	=	fill height [m]
h/R	=	fill fraction
l	=	characteristic length [m]
m	=	azimuthal wave number
m_s	=	slosh mass [kg]
m_l	=	mass of fluid [kg]
n	=	mode number; or cycle number
x	=	excitation direction
R	=	tank radius [m]
Re	=	Reynolds number: $v^2 l/\upsilon$
v	=	velocity [m/s]
w	=	baffle width [m]
x_s	=	slosh mass displacement in x [m]
X_0	=	excitation amplitude [m]
X_0/D	=	nondimensional excitation amplitude
We	=	Weber number: $\rho v^2 l/\sigma$
y	=	vertical direction
α	=	ratio of ullage-liquid interface radius to tank radius
γ	=	damping factor, $\delta/2\pi$
Γ	=	factor relating slosh mass displacement to η
δ	=	logarithmic decrement
η	=	vertical wall height of wave w.r.t. static fluid level [m]
λ	=	$\omega^2 R/g$; square of the nondimensional frequency parameter
ρ_l	=	density of fluid [kg/m^3]
υ	=	kinematic viscosity [m^2/s]
σ	=	surface tension [N/m]
ω	=	frequency [rad/s]
$\omega\sqrt{\frac{R}{g}}$	=	nondimensional frequency parameter
Ω	=	excitation frequency [rad/s]

Acknowledgements

The author would like to acknowledge and thank the following entities and individuals for the invaluable assistance that they have provided in the success of this project to date: Professor Daniel Kirk for being my advisor, Professor Hector Gutierrez for extensive knowledge of instrumentation and mechatronics, the NASA KSC Launch Services Program (LSP) fluids group, in particular Brandon Marsell and Paul Schallhorn, and NASA MSFC ER-42, in particular Doug Westra, Jacob Brodnick, and Jeff West, for guidance and mentoring, the FIT machine shop staff for their assistance in fabricating the test article, and my colleagues in the FIT ASAP and Mechatronics laboratories for their assistance and encouragement in this project. Finally, I would also like to thank my wife, Katie, for her love, support, and encouragement.

This project was funded by a NASA Space Technology Research Fellowship (NSTRF) through the Space Technology Mission Directorate (STMD).

Chapter 1 Introduction

1.1 Background

In the 1950's, NASA became interested in the study of fluid slosh dynamics due to the field's relevance to rockets and spacecraft. In that time, scientists and engineers did not have access to modern computers capable of solving the Navier-Stokes equations, and so they were limited to analytical solutions, experiments, and resulting correlations. By the mid 1970's, avenues for improvement to the field of analytical slosh dynamics were exhausted, and the amount of research in the field decreased.

With the rise of modern computers in the 1980's and 1990's, solving the discretized Navier-Stokes equations became feasible, and computational fluid dynamics (CFD) was born. Since then, CFD has been used extensively to simulate and predict slosh with little experimental data validation. Several mishaps over the last few decades have caused the validity of the CFD-predicted slosh results to be questioned, and the field of fluid slosh dynamics has seen a resurgence since then.

1.2 Motivation

Advancements in in-space, cryogenic propellant storage, management, and transfer science and technologies are key to increasing safety, decreasing cost, and increasing payload mass of NASA's space missions. Since propellant usually

makes up a large portion of a spacecraft's mass, predicting and controlling the motion of it is important. CFD programs are critical to predicting slosh dynamics and finding ways to mitigate these concerns, but CFD programs are complex and require extensive experimental validation before the results can be trusted. Many CFD programs have been validated by slosh experiments for various fluids, but cryogenic fluid slosh experimental data and the corresponding CFD validation is limited, despite the fact that the propellants used by rockets and spacecraft are often cryogens. Non-cryogens may not accurately represent cryogenic liquids, since most of the thermodynamic and transport properties differ greatly. Thus, collecting more experimental cryogenic slosh data, and using it to validate CFD models, is necessary.

1.3 Objectives

The objectives of this research fall into three categories: experimental, numerical, and validation. The experiment objective is to collect fluid slosh data for water and liquid nitrogen in a spherical tank in 1-g relevant for CFD validation. The numerical objective is to perform CFD simulations of select slosh experiments with enough accuracy for validation. The ultimate objective is to show that the CFD can accurately predict the experimental results, thus validating the CFD for 1-g fluid slosh of water and LN_2 in a spherical tank.

1.4 Approach

During the literature review (see Chapter 2), spherical and cryogenic slosh data were being collected from documentation of prior work and to be used for comparison purposes. It was during that process that the lack of cryogenic slosh data, for spherical tanks in particular, was discovered. An experimental test apparatus was designed and constructed to allow for the collection of water and liquid nitrogen (LN_2) spherical tank slosh data (see Chapter 4). Hundreds of different tests were conducted, and each was repeated once to ensure reproducibility.

The approach to the numerical part of this project was less straightforward. CFD modeling is always a trade-off between accuracy and computation time, and examining the extremes is the best way to illustrate this. Direct Numerical Simulation (DNS) solves the complete Navier-Stokes equations without assumptions; while this is the most accurate method, it is not feasible for the computers accessible to the average slosh researcher to run DNS (at the time of this writing). On the other extreme, the Navier-Stokes equations can be simplified to the potential flow equations through various assumptions, including incompressibility and zero viscosity. Many potential flows have analytical solutions, and solving them numerically is easy for the modern computer. However, the potential flow assumptions, particularly the inviscid assumption, are not adequate for accurately modeling slosh dynamics. A practical approach was

chosen for finding an appropriate compromise. If a simulation could be run in less than a week's time with the resources available to me at FIT, I considered it "feasible". The assumptions, models, and mesh size were selected based on this criterion (see Section 5.1.2). Since NASA has more computational resources, NASA researchers should not have any problems running CFD simulations of this fidelity.

The validation objective will consist of comparing the results of the experiments, numerical simulations, and analytical models, with the goal declaring that the CFD methodology used is acceptable for modeling 1-g, lateral fluid slosh of water and LN_2 in a spherical tank. In the evaluation of this objective, it may be determined that the level of accuracy of the CFD is insufficient for modeling fluid slosh. I wish to emphasize that that would still be a useful outcome, as the assumptions, models, and mesh size I chose compare reasonably well to those used in the field, which would imply that the level of accuracy currently used in much of industry for predicting fluid slosh is insufficient.

1.5 Thesis Overview

The thesis is structured as follows: Chapter 2 summarizes all past literature used during this project, Chapter 3 details the analytical and empirical models, Chapter 4 describes the test apparatus, conducted experiments, and experiment-specific

results, Chapter 5 describes the CFD program and methodology, Chapter 6 contains comparisons and discussions of all data, and Chapter 7 summarizes the conclusions and suggestions for future work.

Chapter 2 Literature Review

2.1 Further Motivation

In space, the influence of sloshing liquid propellants may hamper critical maneuvers such as docking of cargo vehicles, pointing of observational satellites, solar-distributing spin cycles, or stability of on-orbit propellant depots. Severe problems with sloshing liquid in spacecraft and rockets have been reported. As an example of the potential slosh impact on rocket performance, a prelaunch review of the CFD propellant-slosh predictions within the second stage of a Delta IV launch vehicle led to a launch stand-down until the issue could be resolved. A worst-case scenario predicted that the liquid hydrogen would not remain constrained in the aft end of the tank and could be ingested into the tank vent-and relief system, resulting in a thrust imbalance and loss of vehicle control. The analysis team concluded that it was imperative to "*determine proper methodology for future Delta IV second-stage propellant-slosh analysis*" [1]. In another example, the NEAR satellite went into safety mode because of an unexpected reaction that was possibly due to propellant slosh after an orbital maneuver which caused a one-year delay of the project [2]. Another example of a dramatic propellant-slosh problem occurred at the end of a yaw maneuver during the Apollo 11 first moon-landing mission, and additional thruster activity was needed for course corrections before the lunar lander finally landed at a different spot than originally planned [3]. Slosh can

increase boil-off via droplets evaporating from contact with warm tank surfaces, increasing the pressure inside the tank and the chances of tank venting. Slosh during transfer can affect the thermal state of the propellant and ullage, which may cause performance issues during tanking and de-tanking operations. In addition to the thermodynamic effects, slosh may have fluid dynamic effects on transfer (and vice versa). Clearly, characterizing slosh dynamics is critical to increasing the safety and reliability of NASA's space missions. Mission planners and designers require accurate and validated simulation tools to understand and predict the effects of slosh on propellant management, thermal management, and vehicle trajectories. Other specific applications that could benefit from this research include general propellant tanks, launch vehicles, on-orbit fuel depots, power reactant storage, and Environment Control and Life Support Systems (ECLSS).

2.2 Review of Technical Publications

While there simply is not enough space here to review all publications relevant to slosh, an attempt was made to cover much of the past and current research.

Starting in the late 1950's, NASA took an interest in fluid slosh dynamics as it pertains to spacecraft and rockets. The NASA SP-106 document [4] compiles and summarizes all of the major analytical and experimental slosh work up though 1965. Many of the primary sources cited in this thesis were found via the reference

sections of that document. An update was released by F. Dodge, one of the major authors of SP-106, in 2000 that contains some more recent information [5]. The last compendia used in this project is Ibrahim's 2005 Liquid Sloshing Dynamics textbook [6] covers essentially everything in [4] and [5], plus more.

Glenn Research Center (GRC) scientists have been researching the behavior of fluids in 1-g and low gravity since the 1950s [7], with a focus in safely and efficiently managing cryogenic propellants. Research into essentially all areas of cryogenic fluid management (CFM) has been conducted at GRC, including acquisition, stratification, thermal control, pressurization, transfer, and slosh. Various ground and flight experiments, many of which occurred before modern numerical modeling was possible, have been conducted by GRC to test the various technologies associated with CFM. The goal is to test a variety of technologies to enable safe and efficient storage and use of propellants for long term space applications, such as propellant depots. Most recently, a non-isothermal cryogenic fluid slosh modeling effort [8] indicated good agreement with CNES low-g slosh data. This is significant because most cryogenic slosh modeling is treated as isothermal due to the intense computational requirements for modeling heat and mass transfer in addition to the fluid dynamics.

Kennedy Space Center (KSC) and Marshall Space Flight Center (MSFC) are also involved in slosh research. MSFC has ongoing spherical tank slosh programs with

water, as well as various CFD validation projects, though few results have been made public. A LN_2, spherical tank, lateral slosh test program was conducted at KSC [9], but the data has not been made public nor used in any model validation efforts to date.

The cryogenic experimental and modeling efforts are not limited to the United States. Two separate teams researching cryogenic slosh in cylindrical cryostats released papers in 2009, one from Germany [10] and one from France [11]. Both examined the thermodynamic effects of cryogenic liquid sloshing.

CFD modeling of spherical tank slosh was recently examined in [12] and [13]; the former uses ANSYS Fluent® and slosh forces from water in a spherical tank for validation data, and the latter uses CFX® to model hydrazine, though with no validation. Aside from slosh force data, wave height or surface data could also be used to compare CFD and experiments. This could be accomplished with arrays of capacitance probes, such as those used in the Facility for Liquid Experimentation and Verification in Orbit project [14], and ultrasonic ranging techniques [15] to estimate the approximate distance from an ultrasonic source to a point on the liquid's surface. Both force data and wave height data were used for validation in this thesis, though wave height data was collected differently than either of those methods.

FIT has conducted research in analytical, numerical, and experimental slosh dynamics over the past few years (see [16] [17] [18]). The experimental efforts have employed shake tables (for restricted DOFs), spin rigs, flights on zero gravity aircraft, and an experiment on the ISS.

Slosh experiments on “zero-gravity” aircraft flights are limited to several seconds of microgravity conditions, and since the slosh tank is constrained to the aircraft, this method does not allow for liquid-tank coupling investigations. FIT partnered with MIT and KSC to perform slosh experiments aboard the ISS using the SPHERES platform: the ISS SPHERES-SLOSH experiment. A pair of high resolution cameras records the movement of the liquid inside a small tank as the experiment is pushed around by the SPHERES robots or the astronauts. This project is sponsored by the NASA Game Changing Development and aims to record data that will be used by engineers on earth to validate CFD programs making them ready for use in designing the next generation of space vehicles.

FIT researchers have used a variety of internally developed and commercially available numerical tools to simulate slosh dynamics. A numerical tool was developed [16] to simulate liquid slosh coupled with tank motion. This thesis uses a more advanced commercial software that has this capability built in.

In summary, no public domain data or papers were found for cryogenic fluid slosh experiments in spherical tanks, nor for CFD of such experiments. It is clear that more research is needed in this area.

Chapter 3 Analytical and Empirical Models

Analytical calculations involving spherical tanks are complicated due to the non-parallel walls [6]. Analytical solutions available for cylindrical or rectangular tanks are significantly more difficult, or impossible, to calculate similarly for spherical tanks. Fortunately, some solutions do exist, as in the case of slosh modes and lateral forces, and certain assumptions can be made to adapt others, e.g. for a ring baffle in a cylindrical tank. Note that analytical solutions are not a major topic for this thesis; they are included for sake of comparison to historical solutions, and thus, their results are simply reproduced here and not derived. The primary sources are included for those interested in their derivations.

3.1 Analytical Modes for a Spherical Tank

Analytically deriving the modes of a spherical tank is difficult. The final equations require extensive numerical integration and the evaluation of the resulting matrix eigenvalue problem; no attempt was made to evaluate these equations. Instead, the first three modes of the m=0,1 azimuthal wave numbers (corresponding to symmetric and antisymmetric respectively if the tank was cylindrical) natural frequencies versus fill fraction curves are extracted and tabularized from Figure 1.12 of [6] and Table 2 and Figure 3 of [19]. While interpolation from tables introduces some error, it saves computation time.

Figure 1 shows the tabular nondimensional frequency versus fill fraction curves for the first three asymmetric and symmetric modes. Symmetric modes are not typically excited by lateral sloshing, so they will be ignored in favor of the asymmetric modes in the following sections.

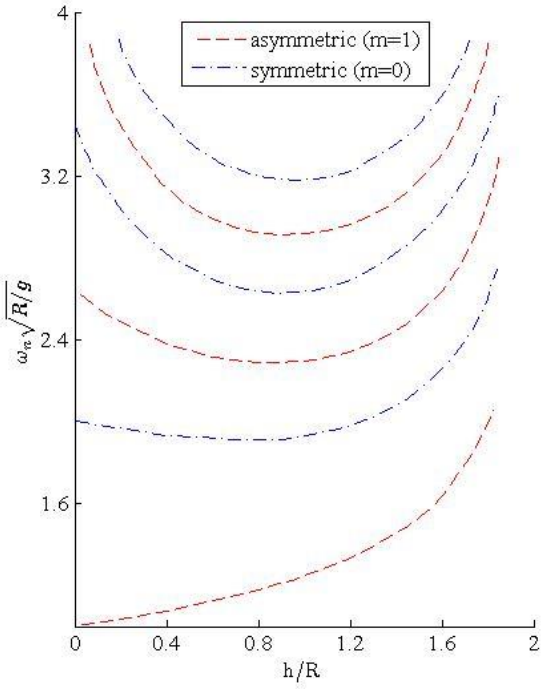

Figure 1. Analytical Modes of a Spherical Tank

3.2 Analytical Solution for Lateral Excitation

Reference [6] presents Budiansky's [20] analytical formulation for the determination of inviscid slosh forces in a spherical container under lateral excitation. While the derivation is too long to reproduce here, the final resulting differential equations are as follows:

$$\frac{d^2\eta_n}{dt^2} + {\omega_n}^2\eta_n = -\lambda_n\alpha\frac{D_n}{E_n}\frac{d^2x}{dt^2}\ , n = 1,2,3 \ldots \infty \tag{3.1}$$

$$F_s = -m_l\frac{d^2x}{dt^2} - \pi\rho_l(\alpha R)^3\sum_{n=1}^{\infty} D_n\frac{d^2\eta_n}{dt^2} \tag{3.2}$$

, where n is the mode, η is the wave height at the wall, and F_s is the slosh force. Note that the discrepancy between [6] and [20] in Eq. 3.1 is due to differing definitions of λ_n. D_n and E_n are calculated from integrals of eigenfunctions of the kernel function. No attempt was made to calculate these coefficients; instead, they were tabularized from Fig. 2.21 of [6], in a similar fashion to the modes versus fill fraction curves and for similar reasons.

All equations are entered, and tables imported, into MATLAB® [21]. For a given amplitude, excitation frequency, and fill fraction, Eq. 3.1 is solved for the first three asymmetric modes (m=1, n=1,2,3) using the ODE45 solver in a `parfor` loop to take advantage of MATLAB's parallel computing capabilities. The required mode frequencies are obtained by interpolation of the nondimensional frequency versus fill fraction tables. Contributions from other azimuthal wave numbers and higher modes are not considered. The contributions of the first three modes are summed and the resulting wall wave height and force versus time curves are computed.

Two common nondimensional parameters are the slosh force parameter $F_{max}/(\rho_l g D^2 X_0)$, where F_{max} is the maximum F_s for a given frequency, amplitude, and fill fraction, and the excitation frequency parameter, $\Omega\sqrt{R/g}$. A slosh force parameter versus excitation frequency parameter curve is computed by looping through the aforementioned process numerous times over a range of frequencies. An example plot for 20% volume fraction of water in the tank considered is shown in Figure 2.

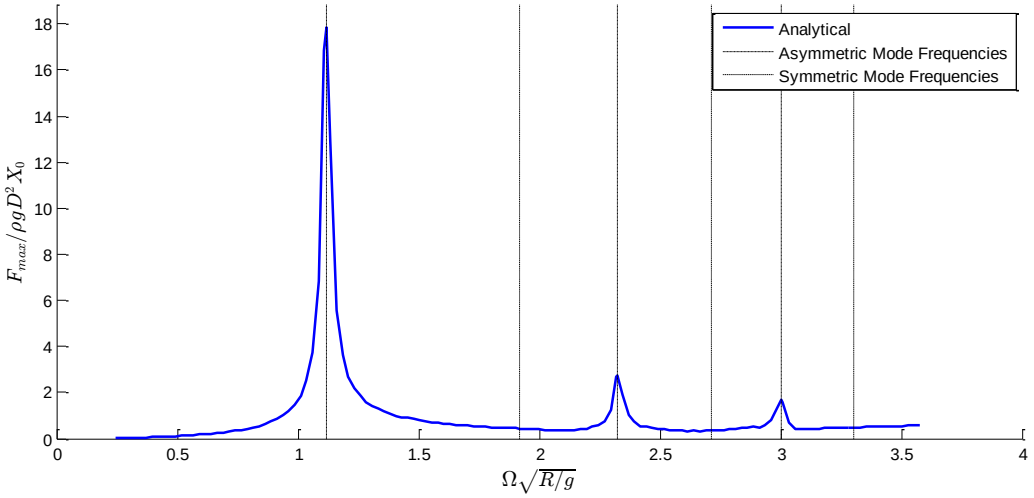

Figure 2. Force Parameter vs. Excitation Frequency Parameter Example

As can be seen in Figure 2, the plots created with this method are imperfect: the resonance peaks are not asymptotic and the curves are not smooth, particularly at higher frequencies. Evaluating at discrete frequencies, table interpolations, and only including the influences of the first three modes are likely the cause of these imperfections. The error introduced by these simplifications has not been quantified, but it is assumed to be small.

3.3 Empirical Damping Correlations

Two parameters are commonly used to describe the damping of a tank and fluid: logarithmic decrement, δ, and damping factor, γ. Logarithmic decrement is calculated from experimental or CFD data via the decay of a relevant parameter:

$$\delta_X = ln\left(\frac{X_n}{X_{n+1}}\right) \tag{3.3}$$

$$\gamma = \frac{\delta}{2\pi} \tag{3.4}$$

, where "X" can be force, wave height, or center of mass displacement, forming a force-derived logarithmic decrement (FDLD), wave height-derived logarithmic decrement (WHDLD), or center of mass displacement-derived logarithmic decrement (CMDLD). An analytical approximation to the damping in a spherical tank was not found in any of the sources reviewed, and few theories exist for calculating it [4]. Various experimental correlations for spherical tanks have been developed for logarithmic decrement based on force, wave amplitude, or other variables. Note that these correlations are not equivalent and rarely agree well. The data that they are based on may have come from slosh that was linear (only first asymmetric mode), nonlinear (many modes), or even exhibiting wave break. Some of these correlations are listed below.

Correlation	Valid Range	Citation	Equation
$\delta_F = 0.131B^{0.359}$	$\frac{h}{R} = 1.0$	[4]	(3.5)
$\delta_{WA} = 0.08347\sqrt{B}\left(\frac{R}{h}\right)$	$0.1 \leq \frac{h}{R} \leq 1$	[4]	(3.6)
$\delta_{WA} = 0.08347\sqrt{B}\frac{1+0.46\left(2-\frac{h}{R}\right)}{1.46\left(2-\frac{h}{R}\right)}$	$\frac{h}{R} \geq 1$	[4]	(3.7)
$\delta = 0.32\left(\frac{1}{G_A}\right)^{0.359}$	$\frac{h}{R} = 0.5$	[6]	(3.8)
$\delta = 0.39\left(\frac{1}{G_A}\right)^{0.359}$	$\frac{h}{R} = 1$	[6]	(3.9)
$\delta = 0.66\left(\frac{1}{G_A}\right)^{0.359}$	$\frac{h}{R} = 1.5$	[6]	(3.10)

, where $B = \frac{10^4}{2\sqrt{2}}\frac{\nu}{\sqrt{R^3 g}}$ and $G_A = \frac{\sqrt{R^3 g}}{\nu}$. Note that Eqs. 3.6 and 3.7 are equivalent to Eq. 2.9a and Eq. 2.9b of [5] respectively when the characteristic length is tank radius.

3.4 Analytical Solution for Baffle Damping

An analytical solution to an annular ring baffle in a cylindrical tank was derived by Miles [22]. The derivation utilizes the fact that a ring baffle is similar to a plate in an oscillating flow, where the primary energy dissipation mechanism is the pressure drag on the plate. The assumptions for this model include: viscous drag is negligible, the static fluid level is above the level of the baffle, the baffle is always fully submerged, the fluid is deep enough to prevent the bottom of the cylinder from affecting the flow, linear (first mode only) slosh, and the direction of the flow is purely normal to the baffle. The final equation for the damping factor is reproduced from [5] below:

$$\gamma = \frac{15(4/3\pi)^2 C_1 A f_d{}^{2.5}\sqrt{\eta w}}{2\sqrt{\pi}(m_s/\rho)\Gamma^2} \tag{3.11}$$

, where w is the baffle width, C_1A is the area blocked by the baffle, f_d relates wave amplitude at the baffle to the wave amplitude, η, and is derived from velocity potentials, m_s is the slosh mass, and Γ is a factor that relates the slosh mass displacement to wave amplitude. This equation has been shown to compare well to experiments as long as the baffle stays submerged; it tends to underpredict damping when the fluid level is close enough to the baffle that it becomes partially exposed. Fortunately, most applications do not require a precise damping value, but a minimum damping value. Ring baffles tend to work even when the fluid level is slightly below the level of the baffle, though this equation cannot be used to predict

the damping when that is the case. Instead, a simple approximation can be utilized such that γ is linearly decreased from its value for static fluid level at the baffle to 0 for a static fluid level 0.8z below the baffle [5].

The equations for calculating f_d, m_s, and Γ are complicated for spherical tanks (see non-parallel wall discussion above), so [5] presents a simple adaption of the above cylindrical method. Instead of trying to derive all of the parameters for a spherical tank, it is simpler to calculate an equivalent cylinder such that the liquid volume above the baffle is the same for the equivalent cylinder as it is for the actual tank. This assumes that the baffle is not located near the top or the bottom of the tank, where the flow can no longer be assumed to be vertical and unaffected by the bottom or top. Comparisons to prior spherical tank slosh data suggest that this is a good approximation. [5]

3.5 Mechanical Analogy

For many applications, such as vehicle dynamics simulations and control analyses, it is convenient to replace the liquid in the tank with an equivalent mechanical model of the mass-spring-damper or mass-pendulum-damper type. Linear sloshing can be accurately represented by a linear dynamical system, and the relevant parameters can be analytically derived for most simple tank shapes, such as cylinders and rectangles. In fact, mechanical models exist for nonlinear slosh, e.g.

rotary, as well [4]. However, the same problem mentioned earlier applies for mechanical analogies of spherical tanks: The nonlinear nature of spherical tanks due to curved walls severely complicates, and sometimes prevents the use of, many of the analytical techniques available for cylindrical and rectangular tanks, though some researches have successfully derived equations for these parameters (see [4] and [23]).

Mechanical analogies were not the focus of this project, and no mechanical system results are included in the results sections. The concept and the following equations for first mode slosh mass and slosh mass displacement are included because they are useful for nondimensionalizing slosh forces (see Section 6.1). Note that only the first mode slosh mass is considered because the higher order slosh masses are typically small.

Since analytically calculating the slosh mass for a spherical tank is difficult, the slosh mass to liquid mass ratio versus fill fraction is tabularized from Figure 6.21 in [4] and Figure 3.4 in [5], and a spline curve fit was generated in MATLAB. The slosh mass was also calculated from 24 forced sinusoidal experiments from four fill levels using the following equation. [24]

$$m_{s1} = \frac{F_S}{X_0}\left[\frac{1}{{\omega_0}^2} - \frac{1}{{\omega_1}^2}\right] \tag{3.12}$$

, where X_0 and ω_0 are the excitation amplitude and frequency respectively, ω_1 is the first mode resonant frequency (taken from the tabularized modes), and F_s is the force amplitude immediately after a continuous, low frequency excitation. These points suggested a correction factor of 0.93 be applied to the analytical slosh mass; after this correction, the experimental values were within +/-5% of the analytical.

Assuming excitation is stopped, the only forces will be the slosh forces, which come from the oscillation of the slosh mass. The slosh mass is used to calculate the slosh mass displacement using the following equations.

$$F_S = -m_{s1}\ddot{x_{s1}} \tag{3.13}$$

$$\ddot{x_{s1}} = -x_{s1}{\omega_1}^2 \tag{3.14}$$

$$x_{s1} = \frac{F_S}{m_{s1}{\omega_1}^2} \tag{3.15}$$

Chapter 4 Experiment

4.1 Test Apparatus Objectives

The objective for the test apparatus is to allow for the collection of spherical tank slosh data with water and a cryogen with enough accuracy for CFD validation purposes, while staying within budget and time constraints. Two types of tests must be performed: forced sinusoidal excitation and damping. Forced sinusoidal tests consist of continuously exciting the tank laterally in 1-axis at different frequencies and amplitudes. Damping tests consist of sinusoidally exciting the tank for a specific number of cycles, quick stopping the motion, and measuring the decay characteristics of the slosh. During those tests, or via post-processing, the following things must be realizable: tank position, tank acceleration, slosh forces, wave height, temperature at several points inside and outside the tank, and high resolution video of the fluid free surface. All aspects of the testing are to be completed within two years of the start date, and within a predetermined yearly budget.

4.2 Test Apparatus Approach

An iterative approach to the test apparatus was adopted, and the second iteration achieved useful results last year [25]. A novel floating tank linear stage was developed, and has been substantially improved this year. The “floating tank”

approach uses a lead screw actuator to push the tank mounted in a frame that is floating on air bearings. Various sensors are used to measure all of the required quantities, including a novel type of continuous fluid level sensor. Further details of the tank, linear stage, and instrumentation are discussed below. While the fluid sensor development caused significant schedule slip, the project stayed within budget and all of the test objectives were met.

4.3 Test Apparatus Design

4.3.1 Selection of Fluids

After determining the type of tests and the shape of the tank that would be used, the next step was determining the fluids to use for testing. Deionized water was chosen for two reasons: 1. there is a large amount past data that can be used for setup validation, and 2. FIT has two large water deionizers. The decision to use LN_2 was motivated by cost and safety. While liquid oxygen (LOx) and liquid hydrogen (LH_2) are the most common cryogenic fluids used in rockets and spacecraft, many safety regulations accompany their use. While LOx slosh testing could have been done on at FIT, it would have required a costly outdoor test apparatus. LH_2 slosh testing was deemed too dangerous for a college campus setting. Acquiring either of these fluids would have been expensive, as FIT does not have the infrastructure in place for them. LN_2 was selected as a safe, inexpensive analog, with the assumption that a CFD program validated for slosh with one type of cryogen is

better than a program not validated with cryogens. As long as appropriate safety precautions are taken, LN_2 testing can be conducted indoors without concern for material compatibility.

FIT has a large LN_2 Dewar with a fill system, and a 20 L Dewar was purchased that could be refilled from the larger Dewar. The 20 L Dewar is used to fill the tank in all LN_2 tests. For water tests, a clean, 5 gallon jug is used and refilled from the deionizer. Funnels are used for both fluids to direct the fluid into the tank, and then removed for testing.

4.3.2 Tank

Properties of the tank used for testing are summarized in Table 1.

Table 1. Tank Properties

Material	3003 Aluminum
Inner radius	0.149 ± 0.001 m
Wall thickness	3 ± 0.2 mm
Flange material	T6-6061 Aluminum
Flange diameter	0.356 ± 0.003 m
Flange thickness	6 ± 0.5 mm (each)
O-ring diameter	3/32 in

A flanged design was chosen to allow for easy disassembly for cleaning and flexibility for testing, e.g. adding baffles, additional tank sections, different internal instruments. The tank was fabricated from two commercial-off-the-shelf (COTS) hydroformed domes. The inside of the tank was sanded with sandpaper up to 1500 grit to remove shallow surface defects and discoloration. The tank was not polished because doing so might have resulted in too much light being reflected back into the top-mounted camera. Flanges were

machined and welded to the domes. After welding, the tank halves were mounted on custom brackets in the mill and the flanges were milled flat. A ball endmill was used to cut an O-ring groove in one of the flanges. Silicon O-ring cord stock is used for water testing. While Indium is ideal for cryogenic seals, it is too expensive. Instead, lead wire is used for LN_2 testing. Since Indium and lead have similar low-temperature properties, it was hypothesized that lead would work just as well as Indium for non-pressurized cryogenic seals. No LN_2 leaks were observed during non-pressure testing. A few small LN_2 leaks were observed for some pressurized tests, but the amount of fluid lost was always less than the amount lost due to boil-off during the test, so the lead seal was determined to have acceptable performance.

A 2.5 in diameter hole was cut in the top of the tank to allow for a camera and lighting. An approximately 0.8 in diameter threaded port was welded on for filling and draining so that the camera would not have to be removed between fill levels. Initially, an aluminum ruler was machined down and screwed to the inside wall of the tank along the forcing axis for measurement of fluid wall height from camera frames. This was replaced by a fluid sensor (see Section 4.3.5). Seven brass thermoprobe pass-throughs were threaded in the tank wall along the ruler at various locations (see Section 4.6.2). PTFE thread sealant tape prevented leaks from threaded holes. The following figure is a picture of each half of the tank. Note that the threaded port had not yet been welded on when these pictures were taken.

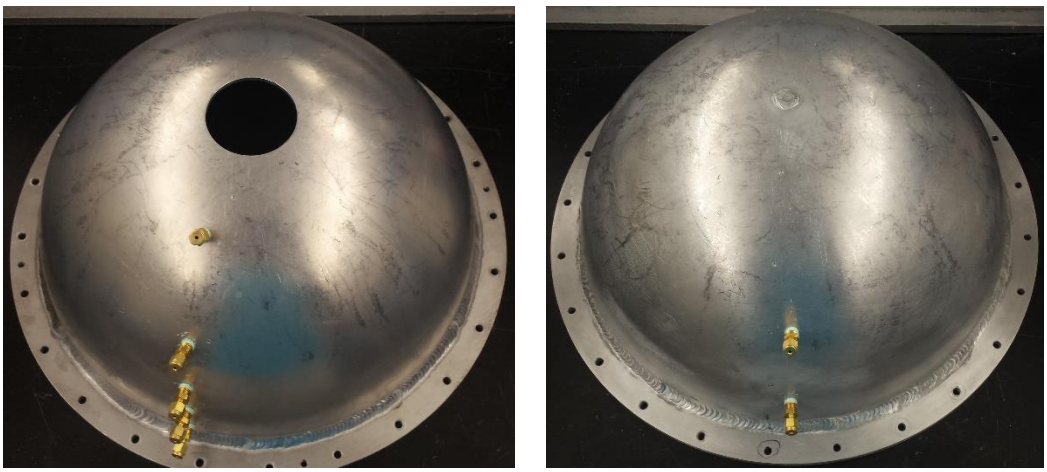

Figure 3. Tank: top half (*left*), bottom half (*right*)

The design of the tank mounting brackets was considered a high priority because a failure of one of these would be catastrophic in terms of safety and experiment damage. The requirements for the tank mounting brackets included: low thermal conductivity, high strength at cryogenic temperatures, high stiffness, and resistance to thermal cycle fatigue. Various materials were considered, but ultimately polycarbonate was chosen due to its common use in cryogenic applications. Finite element analysis (FEA) simulations were performed with room temperature properties to guide the design (no cryogenic temperature mechanical properties of polycarbonate were found). Finally, four tank mounting brackets were machined out of 0.25 in thick polycarbonate sheet. No cracks in the brackets have been observed.

Various types of insulation were considered. Requirements for the insulation included: low thermal conductivity, ability to withstand cryogenic temperatures,

easy to handle, and manufacturability. Although commonly used in space propulsion applications, Multi-Layer Insulation (MLI) was rejected because it is expensive and best suited for vacuum conditions. Aerogel blanket insulation was also considered. While significantly less expensive than MLI, it was ultimately rejected because of cost. 2 in thick insulation domes were CNC machined at FIT from blocks of 2 lb/ft^3 density polyurethane foam (see Figure 3). The outer surface of each insulation dome was covered in aluminized nylon "space blanket" material to decrease radiative heat transfer, though it is unclear how much that helped. Since the first set of insulation domes did not fit well, they were remade with a larger inner radius. Only after the second set was it discovered that machining the cast foam relieves stresses and causes the domes to shrink slightly. Thus, these had to be sanded to fully encapsulate the tank. Slots were cut for the thermoprobes, and an additional hole was cut for the fill port; these were packed with pieces of foam rubber insulation during tests. The hole for the camera was cut during the machining process, as were the provisions for the flanges and flange bolts. Condensation and ice formation around those regions are indicative of significant heat leaks. From measurements of static boil-off rate, the estimated heat leak into the tank at 50% fill level is approximately 77 W, the majority of which was probably through the insulation. Higher boil-off rates were observed at higher fill levels and lower at lower fill levels (see Section 4.6.1). To counteract the high heat leak, a small device similar to a shower head was constructed that drips LN_2

between the tank wall and the insulation during certain tests. Examining plots from the thermocouples and video inside the tank showed that this device worked remarkably well at reducing the heat going into the tank, though no measurements were taken to quantify its effects.

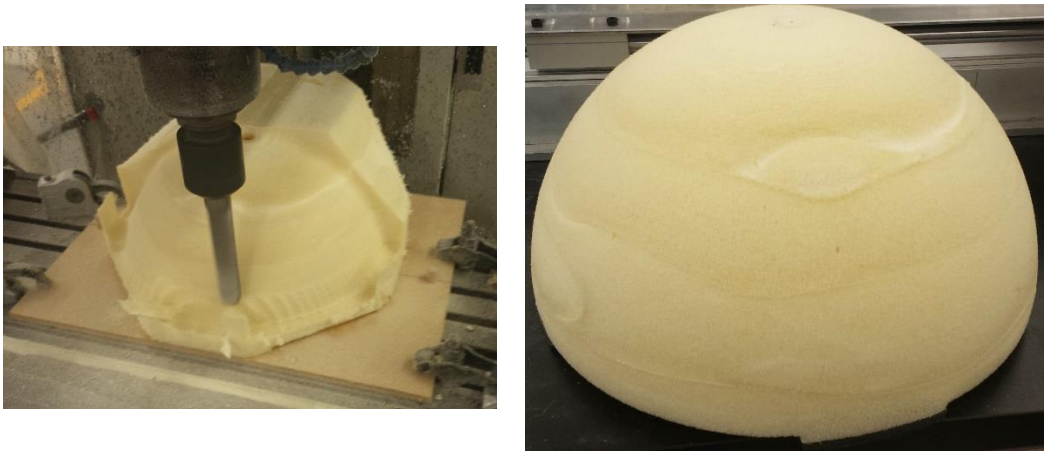

Figure 4. Insulation Machining (*left*), Finished Lower Dome (*right*)

A ring baffle with a width to tank radius ratio (w/R) of 0.125 was fabricated from 0.047 in thick SS304 sheet. That w/R was chosen because past NASA experiments determined that that ratio had the best overall performance [26]. It was designed with a tapered edge to fit in the small gap that is left between the tank halves when a lead O-ring is used. The flange bolts compress the flanges onto the baffle edge, holding it in place. A notch was cut in it for the fluid sensor. Unfortunately, for baffle testing at fluid levels at and below the baffle, this notch tended to cause a jet when the slosh wave impacted the bottom of the baffle. It is unclear whether or not

the jet influenced the accuracy of the fluid sensor. The following picture is of the baffle being installed in the tank.

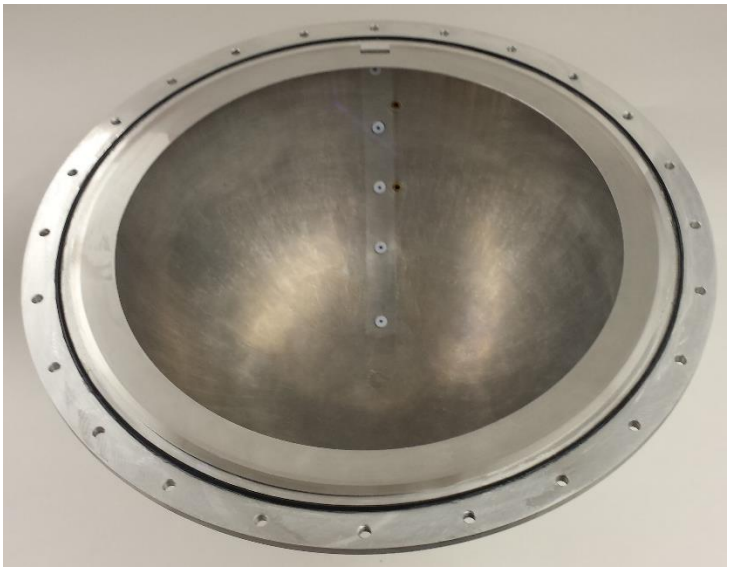

Figure 5. Baffle on Lower Tank Half

Various problems with the tank occurred during fabrication and testing that result in some uncertainty. The inside of the tank is not perfectly spherical. The radius varies by approximately ±1 mm and thickness varies by about ±0.2 mm. The average radius was determined by incrementally filling the tank with a known mass of water until water reached the top of the tank; this mass was converted to volume, and a spherical radius was calculated. Some minor warping occurred during welding of the flanges to the domes, but by milling the flanges flat afterwards, this problem was mitigated. The welding also slightly deformed an approximately 15-20 mm wide ring around the middle of the tank, turning it into a flat cylindrical section. Galvanic corrosion was observed around the brass thermocouples; the

PTFE thread sealant helped mitigate this, but it is still present. Shallow corrosion pits formed in the aluminum after extended (8+ hour) exposure to water. The corrosion products have to be cleaned off between water tests.

4.3.3 Linear Stage

The tank is mounted to a frame fabricated from T-slot aluminum extrusions. The main design requirement for the tank frame was stiffness to prevent mechanical vibrations from affecting the force measurements. Impulse vibration tests were conducted using an accelerometer and hammer to ensure that all structural modes were a high enough frequency and low enough amplitude to be filtered out. A secondary requirement of the frame was low mass to maximize the excitation capabilities of the linear stages. The frame was also designed to be easily adjustable and modifiable.

Tests were attempted on a belt-driven, linear rail style stage in the Mechatronics Laboratory at FIT. However, interactions between nonlinear kinetic and static rail friction, belt stretching, and the belt sprockets result in low frequency, high amplitude mechanical vibrations on the order of the slosh forces trying to be measured. This problem prevented accurate force data from being recorded; thus, a new stage was designed.

The novel “floating tank” concept for slosh testing utilizes air bearings to support the vertical loads. The air bearings float a few microns above glass sheets using high pressure air, which minimizes friction. This concept is novel in the sense that using air bearings to support a tank for slosh applications has not been seen in the literature. It has many advantages over the more common linear rail and pendulum style slosh test setups. As mentioned earlier, linear rail based test setups suffer rail friction. While hanging pendulums have less friction than linear rail setups, they are limited to small amplitudes to prevent vertical motion and are often multiple stories tall, requiring special facilities to house them. In addition to the lack of friction and no ball bearings to maintain, a floating tank test setup has the ability to perform multi-DOF testing. This can be accomplished by decoupling the actuator from the floating frame and allowing the frame and tank to traverse across a flat floor (see Chapter 7). With the addition of propulsion and control modules, spacecraft dynamics under the influence of fluid slosh can be experimentally investigated on the ground.

In the current, 1-DOF application of the floating tank implementation, a lead screw-based actuator is used for excitation. Using a lead screw eliminates most of the backlash and vibrations that were seen in the belt-driven actuator. The actuator is driven by a Beckhoff combined programmable logic controller (PLC) and motor power supply. The controller was tuned via trial and error until acceptable position

performance was obtained. The maximum excitation amplitude error in sinusoidal testing was measured to be 4%, with an average error of 1%. Even though the floating frame had essentially no friction, the lead screw actuator did. Because of the strict position requirements of the controller and the lead screw friction, the force waveforms had significant high frequency pulses/noise. "Significant" is relative to the excitation frequency and amplitude, but the lower acceleration tests had force spikes of similar amplitudes to the main force waveform. This noise was of a high enough frequency to be filtered out, and it is unlikely that it significantly affected the results. A panic stop button and limit switches were implemented as safety precautions.

The following figure is a picture of the complete test setup, including instrumentation. Specifically, this is the setup for LN_2 with no baffle. The tank is inside the aluminized nylon-covered insulation domes. Visible on the right is a moisture condensation plume from the cold N_2 boil-off venting out of the vent valve. Tracing the ice-covered vent line back to the tank shows the location of the vent port, which is also the fill port. All forced excitation testing was done with the same system mass; ballast was added to account for no insulation or vent system with water, and no baffle for normal testing. One of the two ballast plates (marked "ballast") that account for the baffle mass is visible in this picture. The camera is

tucked inside the bundle of optical fibers at the top of the tank. The accelerometer and second load cell are hidden by the frame.

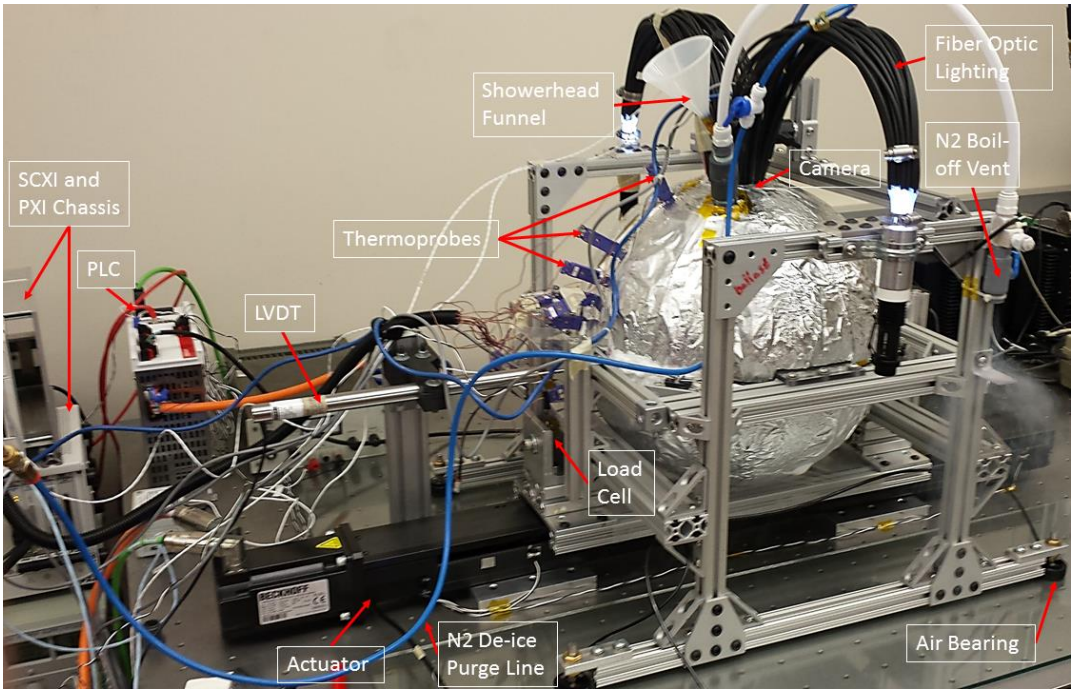

Figure 6. Complete Test Setup for LN_2

Great care was taken to align and level all parts of the setup and instrumentation. The actuator is bolted to a self-leveling optics bench style table, which was adjusted to within 0.1 deg using a precision digital level. The air bearings were adjusted until the frame was level to the glass within 0.002 in. Any parts of the frame that touch or could affect the alignment of sensors was machined to as tight a tolerance as possible. The sensors and instrumentation in Figure 6 will be discussed next.

4.3.4 Instrumentation

The instrumentation consists of a data acquisition system, sensors, and a camera. A block diagram of the instrumentation system is presented in Figure 7.

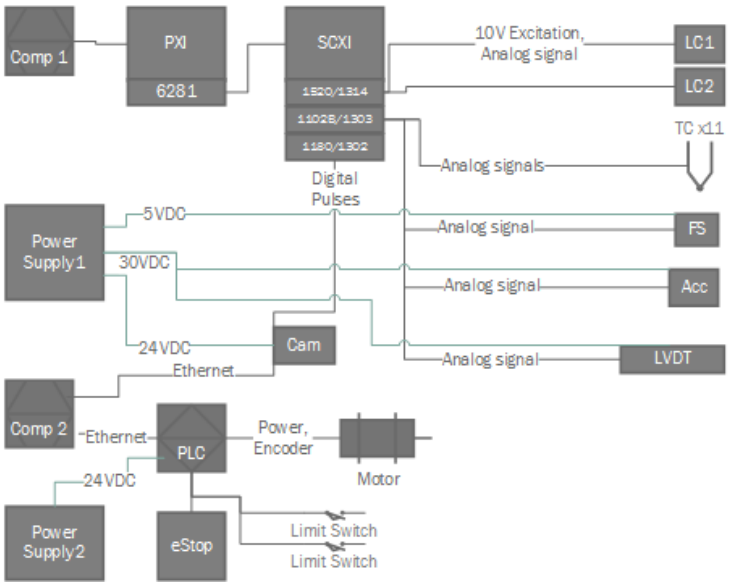

Acc	Accelerometer
Cam	Camera
Comp	Computer
eStop	Emergency stop button
FS	Fluid Sensor
LC	Load Cell
PLC	Beckhoff PLC
PXI	PXI Chassis
SCXI	SCXI Chassis
TC	Thermocouple

Figure 7. Instrumentation Block Diagram

4.3.4.1 Data Acquisition System

The data acquisition system (DAQ) consists of a National Instruments (NI) PXI chassis, PXI-6281 M series DAQ card, SCXI chassis, SCXI-1520 load cell module with a SCXI-1314 terminal block, SCXI-1102B thermocouple and analog input module with a SCXI-1303 isothermal terminal block, and a SCXI-1180 feed-through. The PXI 6281 is an 8 channel, 18 bit, 500 ks/s DAQ card; it is connected to the SCXI chassis, which multiplexes all of the signals from the two SCXI

modules into the AI0 channel of the PXI 6281. The 18 bit ADC ensures that the error due to the DAQ card is negligible.

The SCXI modules are around 20 years old. While a newer data acquisition system would have reduced uncertainty, it was simply not in the budget. Hardware checks were done to ensure that the modules were still working properly. The SCXI 1102B/1303 module is used with all of the sensors except for the load cells. The channels used by the thermocouples were calibrated using a precision Omega thermocouple simulator with 0.1 °C accuracy; the calibration constants were placed in a csv file for correction during post-processing. Unfortunately, I did not have access to instrumentation accurate enough as per the SCXI calibration manuals to perform a hardware calibration, which overwrites the calibration constants stored in the hardware's' memory. However, basic checks and tests showed that all SCXI module channels were functional.

The 1102B contains a 3 pole low-pass Butterworth filter with a fixed cutoff frequency of 200 Hz. The phase delay due to this filter was estimated using the `grpdelay` MATLAB function to be less than 1 ms. The 1520 contains a 4 pole selectable Butterworth filter. When used as a low-pass filter, the frequency is selectable between 10, 100, 1000, and 10000 Hz. 100 Hz was used for all of the testing. This resulted in approximately 4ms of delay between the load cells and the other instrumentation. This delay is discussed more in Section 4.5.

The SCXI-1180 feed-through allows for direct access to the PXI-6281's pins. A digital channel was connected to the camera as a hardware frame trigger. A pulse train of a selectable frequency was sent to the camera to trigger frame capture.

All analog and digital tasks are synchronized at the hardware level via a shared sample clock. The maximum sample rate of the system was not tested, but it was calculated to be above 2 kHz. All testing was done with a sample rate of 1 kHz.

4.3.4.2 Motion and Force Sensors

A Sensotec accelerometer is aligned with the forcing axis. It uses an inline amplifier and is calibrated using earth gravity as a reference. A Sensotec DC linear variable differential transformer (LVDT) with four inches of travel is used for position measurement. It was calibrated using a digital micrometer with 0.00005 in precision. Both sensors were powered from a 30V DC power supply and the analog outputs are wired to input channels in the SCXI-1102B/1303 module. Differentiating dynamic LVDT measurements produces excellent agreement with the accelerometer data, thus verifying that both sensors work properly.

The primary driver for load cell selection was cost. Systems capable of measuring triaxial forces and moments were too expensive. Thus, it was decided to only easure forces in the forcing direction. A piezoelectric force ring with a high enough load rating was used in an earlier iteration of the test setup. However, piezoelectric

force sensors tend to suffer from nonlinear DC drift when loaded at low frequencies (even when properly preloaded), so it was not used in this iteration. Strain-gauge based load cells do not suffer from the same problem, and after some research, Futek seemed to have the best prices on low profile strain gauge-based load cells. Two Futek LRF350 200 lb load cells were purchased to measure force in the axial direction. One is placed on either side of the frame to allow the frame to be driven symmetrically, which eliminates moments about the axes perpendicular to the forcing axis and minimizes vibrations. Maximum stress calculations, which take into account off-axis loads, were done that showed that two of the LRF325-75lb load cells would be able to handle the maximum worst cases forces without being damaged (sudden stage halt). However, at the time of purchase, these were not in stock and would have been far more expensive, so the 200 lb models were purchased.

Unfortunately, using the 200 lb load cells effectively cut the accuracy by a factor of 2.7 since the higher range would not be utilized. Aside from the loss of accuracy, the biggest problems this substitution caused were from the increased nonlinearity. Low force sinusoidal excitation tests had somewhat unreliable force readings due to the load cell's nonlinear deadband region (see Section 4.5). More pre-loading of the load cells in compression might reduce the deadband region. Another improvement that was thought of after testing was combining the signals prior to the DAQ.

Currently, both load cells are excited by, and signals read by, the SCXI 1520 module, and the total force is computed in post-processing. A better way to do it might be to invert one of the signals and wire it in parallel with the other signal into one channel of the SCXI 1520 module. This would eliminate the other channel and ensure that the two load cell signals are synchronized. However, this would make accounting for slight differences in the load cells more difficult.

The calibration tables that came with the load cells are linearly interpolated by the LabVIEW VI to convert mV readings to lbf, and then a conversion factor is used to convert to N for the output csv data file.

4.3.4.3 Thermocouples

Thermocouples were used to gather data relevant for measuring fluid height, ensuring thermal equilibrium, characterizing stratification, and to try to capture slosh. Seven 0.06 in diameter, stainless steel, grounded junction, E-type thermoprobes penetrate the tank wall with their tips approximately 1.5 mm inside the inner wall. Positions correspond to various volumetric fill fractions (see Figure 8). A carbon fiber tube between the pass-through and the thermoprobe connector stiffens each probe. Four additional, adhesive-patch-type thermocouples are placed outside the tank. Two are adhered directly to the tank wall using polyimide tape. Two more are located on the outside of the insulation at the same elevations, but rotated 90 deg so that they are not adhered over the insulation gap.

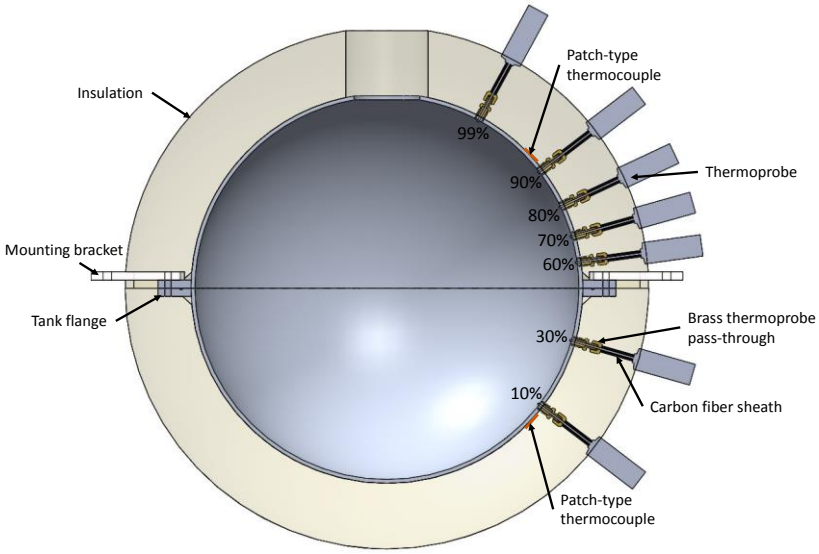

Figure 8. Tank CAD Cross-section.

While the SCXI thermocouple channels were calibrated, the thermocouples themselves were not. At room temperature, they are usually within 1 °C of each other, and within 3 °C while immersed in LN_2. The SCXI-1102B was chosen specifically because it has a higher cutoff frequency filter than the 1102A, which should allow for the capturing of slosh events with the thermocouples (see Section 4.6.2).

4.3.4.4 Noise

All avenues for electrical noise reduction were investigated. All sensors' shields are grounded, and the DAQ and sensor power supply grounds are isolated from the motor controller's ground. Ground loops were avoided wherever possible.

4.3.4.5 Imaging and Pressurization

A 5 MP IDS® Ethernet machine vision camera was mounted above the tank to capture images of the fluid surface. The camera was controlled via a custom C code that grabs frames from the camera when it detects a pulse on its hardware trigger pin. The maximum frame rate achieved was 34 fps at approximately 1 MP resolution. Frame rate was limited by the Ethernet bandwidth and camera exposure. Most tests used a frame rate of 30 fps.

Imaging inside of a small opaque tank was challenging. Small slosh tanks are typically made transparent to allow the placement of cameras and lighting far enough away to capture images of the fluid surface without the use of distorting wide-angle lenses. However, metallic tanks or cryostats are required for cryogenic fluid slosh testing. Since a cryostat was out of the budget, a metallic tank was used, which restricts the camera location to the ullage. Small opaque tanks, like the one used for this project, require a lens with a large field of view in order to see the entire inside of the tank. Thus, a fisheye lens was used for all tests, which skewed depth perception. An image rectifying script was written in MATLAB to attempt to correct for the distortion caused by the fisheye lens. It did not seem to reduce distortion significantly, so it was not used. The following figure is a picture of the camera and lens used mounted on the beam that holds it in place during testing.

Figure 9. Camera with Lens Heater Installed

An additional difficulty with opaque tanks is lighting. The brightness of the light is inversely proportional to the frame exposure time, which directly influences motion blur. Thus, a brighter light will result in less motion blurring. Besides brightness, other requirements for the lighting include: low heat production, wavelength(s) near the highest sensitivity wavelengths of the camera, and ability to withstand cryogenic temperatures. A ring of white LEDs were used in previous test setup iterations. While LEDs can operate while submersed in LN_2, deep thermal cycling causes failure. Thus, the LEDs were replaced with a fiber optic lighting system. Two 1000 lumen LED flashlights are connected to approximately 60 strands of 3mm optical fiber (see Figure 10 below). While the lighting was more reliable with this method, it was not as bright and tended to be more spot-like, both of which caused poorer quality images.

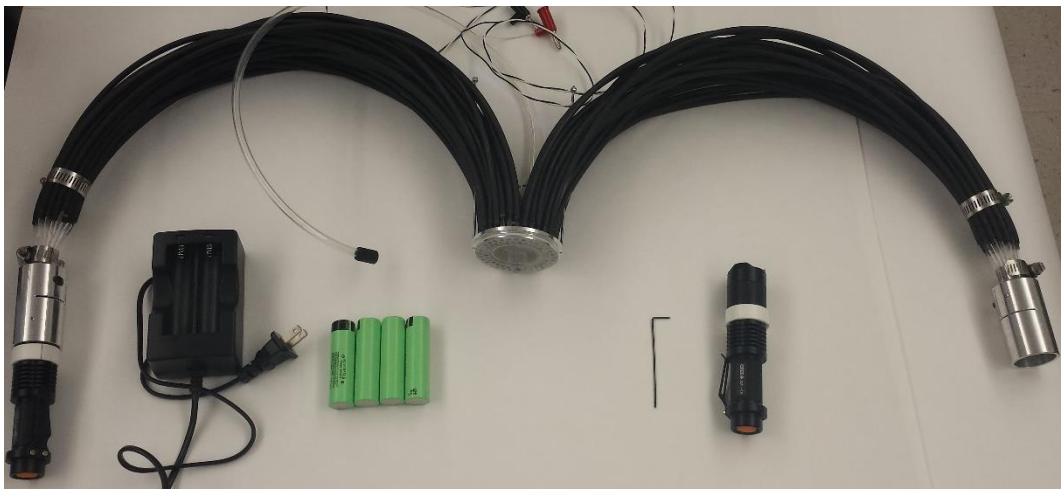

Figure 10. Fiber Optic Lighting System and Pressure Cap

The optical fibers were glued into a specially machined aluminum cap using an epoxy specially formulated for optical fiber applications. A laser cut plastic lens covered the hole in the cap for the camera to prevent splashing fluid from hitting the camera. This lens tended to frost during LN_2 testing, so a N_2 purge was added from a large compressed N_2 bottle, a regulator, and a few small hoses (see Figure 6). A PTFE O-ring was placed in a groove around the cap to provide a seal against the hole in the tank. This, coupled with the vent relief and valve system shown in Figure 6, allowed the tank to self-pressurize during LN_2 testing. By pressurizing the tank, boiling could be temporarily halted to test its effects on damping (see Section 6.1). Unfortunately, weeks of deep thermal cycling caused stresses in the tank material from the hydroforming process to release, which deformed the hole in the tank a few thousandths of an inch and caused the cap to develop a small leak. Despite the leak, the pressure increase was enough to stop boiling.

4.3.5 Fluid Sensor Development

4.3.5.1 Background

One of the test apparatus objectives was to measure fluid height at the wall during sloshing. Last year, 1000's of images from the camera were manually examined to determine fluid height via the ruler inside of the tank. This method was determined to be impractical for large numbers of tests. Computer vision tracking of the fluid interface along the ruler was attempted, but, because both water and LN_2 are clear, there was not enough contrast for the algorithms to work. While the water could have been dyed, LN_2 tends to freeze any dyes or coloring agents that come in contact with it. Thus, using a sensor capable of accurately measuring slosh wave height along the wall of the tank with both water and LN_2 was necessary.

An extensive search of current fluid sensors was conducted with the goal of finding one that could be adapted to this application. Many types of fluid level sensors were considered, including 3D scanning technology and ultrasonic sensors. FIT has previously demonstrated high frame rate 3D point cloud capture of slosh of IR-opaque liquids, but the device was too large to fit into this tank and would not have worked at cryogenic temperatures. Ultrasonic range finding sensors, while adequate for static level measurements, do not have the necessary precision for wave height measuring. Another type of fluid sensor technology utilizes the fact that most fluids and gasses have different dielectric constants. These are called capacitive fluid

level sensors, because they measure the change in capacitance due to a change in the average dielectric of the media filling them.

Most fluid level sensors are simple switches, i.e. the sensor only recognizes if it is covered in fluid or not. A few commercial examples of continuous fluid level sensors capable of measuring fluid level as a function of time were found. The only ones found for cryogenic liquids were based on concentric cylindrical plates that stick down into a cylindrical tank like a mast. The level of the fluid is determined from the capacitance between the cylindrical plates, which is dependent on how much fluid is filling the space between the plates. Even if these could be adapted for fluid level measurement along the wall of a tank, the bandwidth of the sensors was unpublished. Since they are mainly used to monitor the level in storage tanks, it is unlikely that they had high enough bandwidth for slosh applications. Continuous fluid level sensors for measuring fluid level along the wall of a non-conductive tank were also found. These are based on a pair of coplanar plates that sit on the *outside* of the container. The electric field arcs from one of the plates, into the container (and the fluid), and then to the other plate. When the fluid changes height in the container, it changes to electric field, and thus the capacitance. The advantage to this method is that the fluid does not contact the sensor. No commercial application of these sensor for cryogenic liquids was found, probably because most cryogenic fluid containers are metallic, and conductive materials

shield the electric field from the fluid. While possibly useful for glass cryostats, external coplanar capacitive sensors could not be adapted to this application.

No fluid level sensors capable of measuring water and LN_2 slosh wave height along the wall of a conducting tank were found. A sensor development program was undertaken at FIT with the goal of creating one that fits these requirements. With the help of a Dutch electrical engineering intern, a capacitive fluid level sensor that met this objective was successfully created.

4.3.5.2 Design and Development

The first step was to design a circuit capable of measuring variable capacitance. A custom circuit was attempted first, and while it could read static capacitance accurately, it could not measure variable capacitance well. Many of the major integrated circuit (IC) manufacturers sell capacitive sensor ICs, some specifically for fluid sensor applications. These are called capacitive-to-digital-converts (CDCs) or capacitive-to-analog-voltage converters (CAVs). The former communicate over I^2C or SPI, while the latter output an analog voltage proportional to the measured capacitance. CDCs suffer less from noise due to using a digital communication protocol, but because interfacing (and synchronizing) I^2C or SPI sensors with NI hardware is difficult, a CAV chip was selected. After breadboard prototyping, a PCB was designed and ordered. Due to the dissimilar nature of the dielectrics of deionized water and LN_2, two circuits had to be made that differed only in the

values of the tuning resistors and capacitors. The following picture is of one of the PCBs.

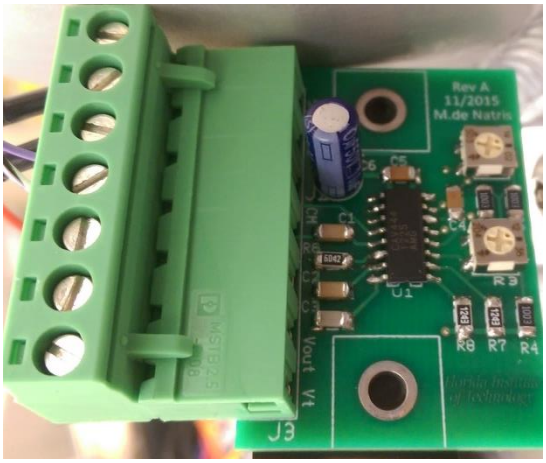

Figure 11. Fluid Sensor PCB

The sensor is power from a 5V DC power supply and the analog output is wired to an input channel in the SCXI-1102B/1303 module. Specifics of the circuits are not included because they are out the scope of this thesis, and I did not personally design them. All of the electrical design and circuit fabrication was done by the electrical engineering intern.

Because of the tank wall is conductive, the capacitor part of the sensor has to be mounted inside the tank. While some epoxies were tested that could withstand repeated thermal cycling to LN_2 temperatures, a less permanent solution was desired so that the sensor could be removed from the tank. High strength neodymium magnets were tested, but magnets strong enough to hold the sensor to the wall during slosh were large enough to significantly affect the flow. Ultimately,

nonconductive nylon screws with custom PTFE spacers (the spacers can be seen in Figure 5) were used to hold the final sensor in place.

Two capacitor geometries were considered: parallel plate and coplanar. Coplanar capacitors have several advantages over parallel plate capacitors. Parallel plate capacitors require two plates with a spacer between them. Because coplanar capacitors are only one plate tall, they do not intrude on the fluid volume as much. They also do not suffer from viscous lag or capillary effects. Because the plates in a parallel plate capacitor are so close together, and because fluids are not inviscid, it takes time to fill the gap between the plates; this time is seen as a lag. If the surface tension of the fluid is significant, and if the contact angle of the fluid-gas-solid interface is not 90 deg, there will also be capillary effects. Assuming similar surface properties as the tank wall, coplanar capacitors do not suffer from either of these problems. However, coplanar capacitors are harder to construct and are approximately 10 times less sensitive (according to prototype testing). While the lower sensitivity is not a problem for water due to its high dielectric relative to air, the difference between the dielectrics of LN_2 and N_2 is small. So small in fact, that the CAV chip purchased could not be made sensitive enough in the coplanar configuration to accurately read changes in fluid level. Another problem with coplanar capacitors is coupled with the chip selection. The CAV chip selected references one of the capacitor plates to ground. Because the tank is grounded

through the grounded junction thermoprobes, this meant that one of the coplanar plates and the tank were at the same potential. This reduced the effectiveness of the sensor because the not-grounded plate acted like a parallel plate capacitor with the tank. Even if the thermoprobes were electrically isolated so that tank would be at a floating potential, the plates would still form an electric field with the tank wall, reducing the effectiveness of this type of sensor. A CDC chip exists that has an active shield that could be connected to an ungrounded tank to mitigate this problem, but it was too late by the time this was discovered to completely redesign the sensor circuitry, and the sensitivity problem with coplanar capacitors in LN_2 remained. After an extensive design and prototyping process, a parallel plate geometry was ultimately chosen, where one of the plates would be the tank wall, and the other would be a thin aluminum strip spaced off the wall enough to minimize capillary effects. It was assumed that the spacers would not affect the results and that the lag would not be substantial.

Because deionized water is mildly conductive, the sensor plate would have to be electrically isolated from the tank wall. While it would be fairly simple to coat the plate in a rubber, plastic, or polyimide tape, one of the requirements was that the sensor had to work with water *and* LN_2. The normal boiling point of LN_2 is 77 K, which is cold enough to cause thermal stress cracking of most rubbers, plastics, and adhesives. Finding a combination of plastics and sealants that would keep water out

and not crack at 77 K took about 6 weeks. Even then, the sealant usually has to be redone when switching from LN_2 to water.

A thin adhesive ruler with mm markings was added to the sensor for two reasons: sensor calibration and verification with images.

The following pictures are of the final sensor installed in the top half of the tank.

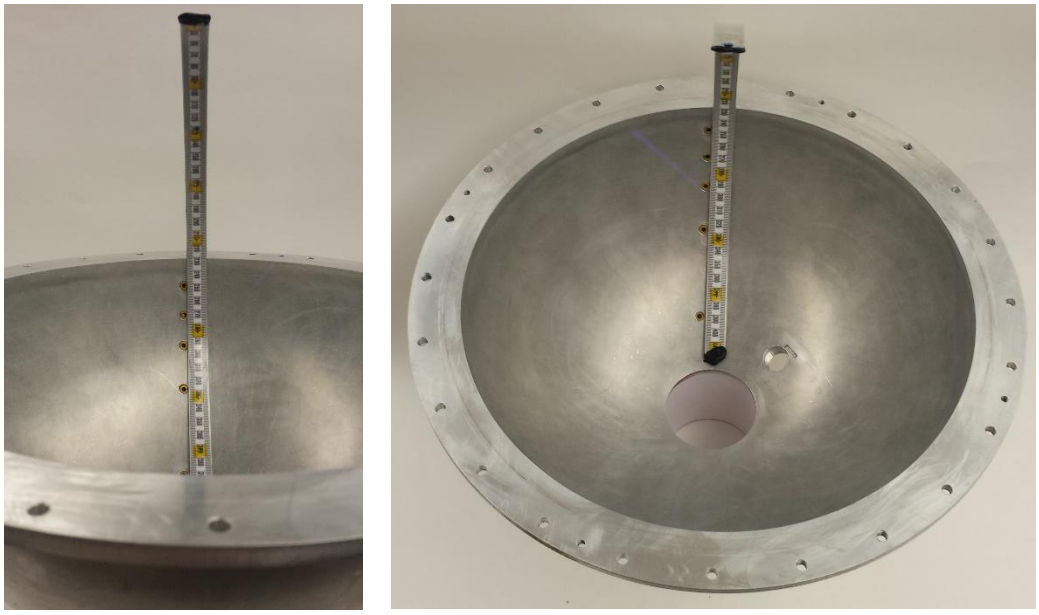

Figure 12. Final Fluid Sensor Installed in Tank

4.3.5.3 Capabilities

The sensor meets the objective of being able to measure the fluid height along the wall of the tank with water and LN_2 for slosh applications. Results from this sensor are presented in Chapter 6. The exact accuracy of the sensor is difficult to quantify. After all error correction schemes are applied (see Section 4.3.5.4), a best guess of

the accuracy is about ±10 mm for LN_2 and ±5 mm for water. While the accuracy may not be particularly good, the precision is better, meaning that small relative measurements with the sensor are useful, even if the absolute level is incorrect.

Aside from measuring slosh wave height, the fluid sensor was able to measure the oscillations due to the turbulent natural convection boundary layer along the wall of the tank. These measurements are available at the start of every LN_2 test and in the LN_2 fluid sensor calibration tests. While they were not used in this project, these measurements could be useful for non-isothermal CFD validation or empirical tuning of natural convection boundary layer models in tanks.

4.3.5.4 Current Problems, Solutions, and Future Work

The development of the sensor was a major effort and took approximately three months longer than planned, and was thus the largest schedule stressor. Many problems still exist with the sensor, and the solutions to them should be considered future work, though some work-arounds and corrections were found for this set of data.

One major operational problem is the aforementioned seal cracking and leaking. The biggest consequence of this is the time lost due to sensor maintenance when switching from LN_2 to water. The materials used in the construction of the sensor need another few iterations. One alternative would be to have one sensor for water

and one for LN_2. Because LN_2 is not conductive, the sensor plate would not have to be electrically isolated from the fluid.

Error from parasitic capacitance, mainly from the wire leads, is significant. Slight changes in the distances between the leads cause large changes in the signal. Coaxial cable was tried because it has a constant spacing between the conductors and thus, a constant capacitance. However, the coaxial cable's capacitance was large (relative to the signal) due to the concentric nature of the conductors, and the fluid sensor circuits could not offset an additional capacitance that high. Two conductors separated by three others from a piece of ribbon cable was the cable ultimately used. While twisting the ribbon cable caused noticeable changes in capacitance, as along as the cable was secured so that is could not move during testing, the parasitic effects of the cable were minimal (~3.6 pF). The best way to mitigate the wire lead problem would be to use shorter wire leads. However, the circuit is also sensitive to temperature (holding a finger on the CAV chip causes a noticeable change in reading), so the circuit could not be located near the tank during LN_2 testing. The fluid sensor circuit is taped under the fiber optics behind the funnel in Figure 6. Enclosing the circuit in a small temperature controlled enclosure would solve this problem.

An interesting phenomenon was observed when attempting to calibrate the sensor with water for the first time. The sensor readings tended to drift upwards with time,

indicating an increase in capacitance. Over an hour, this drift could correspond to a change of more than 5 mm in water, which obviously was not physical. If the fluid sat static for more than 15 minutes, it was observed that sloshing the fluid tended to cause a negative offset in the static level of the fluid approximately equal to the positive drift during the time the fluid was stagnant. While the water used was deionized, water is an excellent solvent. It is hypothesized that the water dissolved some residues left on the tank wall or fluid sensor, causing ions to be present in the water. These ions would then tend to drift towards the oppositely charged plate of the capacitor, similar to the electrochemical ion layer phenomenon. Agitation of the fluid would then cause a disruption in these layers. The exact cause was not investigated further since a solution was discovered: do not let water sit in the tank un-agitated for more than 15 minutes. Oddly enough, a similar drift, though smaller in magnitude, was observed with LN_2. LN_2 is a poor solvent, and the natural convection currents from heat leaking into the tank would likely prevent the build-up of an ion layer should ions be present. Instead, this was attributed to a thin layer of ice that tended to form on the parts of the tank wall not submerged. The moisture that formed the ice was from the air inside the tank before testing started. Sloshing would sometimes disrupt the ice layer. Since the effect with LN_2 was small compared to the calibration error, it was ignored.

Calibrating the sensor for water and LN_2 was challenging. Due to the aforementioned drift phenomena, as well as slight changes in plate spacing when the tank was taken apart and reassembled between tests, sets of calibration data had to be taken for every test. No attempt was made to apply calibrations during data collection. Instead, the set of calibration data for that test day was compiled with a MATLAB script, and a linear fit was calculated to obtain a slope and offset to convert from voltage to arc mm up from the bottom and around the tank wall. The conversion between capacitance and arc mm is expected to be linear because the plates are curved with the tank wall. For water, calibration data consisted of filling the tank with a known volume of water (measured with a scale with 0.5 g accuracy) and using geometry to calculate the correct arc mm assuming a spherical container. Prior to real testing, these types of calibration tests were also used to calibrate the ruler. By making note of the ruler measurement at the known fluid volumes, the exact offset of the ruler along the arc of the tank wall could be determined. However, because the ruler is located on a radius a few mm smaller than the tank wall, a slope factor was also necessary, thus forming a linear relationship between ruler arc mm and true arc mm. This was important for LN_2 calibration tests because an exact volume or mass measurement of LN_2 was impossible due to boil-off while filling the tank. The internal ruler was used to gauge LN_2 volume for calibration (and during tests). Unfortunately, the convection current ripples on the free surface meant the accuracy of the method could be no better than the height of the ripples,

which ranged from about 3-5mm depending on tank level. These readings were converted to true arc mm for deriving the calibration coefficients using the MATLAB script mentioned earlier. Thus, each day of tests had its own set of calibration coefficients for converting fluid sensor voltage to true arc mm. Vertical height from the bottom of the tank was calculated using geometry assuming a spherical container shape. While creating calibration coefficients for each set of tests increased accuracy, it is clearly inconvenient. The sensor circuit needs an auto-calibration feature. Some of the CDC chips had additional capacitor channels that could be used for auto-calibration by having a separate set of sensor plates that is always submerged, but the CAV chip used for this sensor did not have that feature.

The CAV chip has a theoretical bandwidth to the 1000's of Hz, and it was tested using a shaker actuator to oscillate the plate distance to a bit over 100 Hz. That is more than sufficient for a slosh application. However, the parallel plate lag issue discussed early caused the effective bandwidth to be < 1 Hz. A system identification model was created for the sensor for water and LN_2 using MATLAB's System Identification toolbox. This process involved reading the fluid level off of the ruler from hundreds of images of slosh tests to obtain a set of "true" signals. A MATLAB script was written to partially automate that process by pulling up images and applying a pixel scale that allowed the user to simply click

on the fluid interface on the ruler. These were compared to the calibrated signals from the fluid sensor. 1-pole 1-zero lead compensators for each fluid were created from the system model and were applied to the data during post-processing, effectively increasing the sensor's bandwidth and allowing the sensor to be used for the collection of slosh data. The lag is fluid dependent because the viscosity of LN_2 is approximately five times lower than that of water. If the sensor plate was perfectly spaced from the tank wall, these lead compensators would probably have been sufficient. However, due to the weld-deformed cylindrical region around the center of the tank, the plate spacing is decreased by approximately 25% on average in that region. This causes a nonlinearity in the lag for slosh waves that cross a band about 20 mm wide on either side of the 50% line. The effect was minimal with LN_2 due to its low viscosity, but it resulted in significant error in the 40%, 50%, and 60% volume fraction water slosh tests. An empirically designed amplitude stretching algorithm was designed to partially correct for the increased attenuation with water around 50%. While this algorithm certainly helped, the fluid sensor error around 40-60% range should be considered higher than it is for the rest of the tank.

The error due to the circuit's capacitance measuring electronics and the DAQ ADC are likely minimal compared to the other sources of error discussed above.

In summary, there is much work to be done before this sensor can be commercially viable. However, for this application and possibly other research applications, the sensor is a significant improvement over reading the fluid levels manually from 1000's of camera frames, and it meets its objectives.

4.3.6 Software

A LabVIEW Virtual Instrument (VI) program runs the data acquisition of all sensors except for the camera. While LabVIEW generates the pulse train for the camera to ensure that the frames are synchronized with the data, a custom, multi-threaded C code running on a separate computer handles the actual frame saving.

The Beckhoff motor controller is run and programmed using TwinCAT3® software. Due to the complexity of the program, the motor controller was not programmed. Instead, a built in sinusoidal oscillation function was used. An Excel sheet was written to translate the position waveform parameters into the velocity input parameters required by the function.

4.3.7 Potential Test Setup Improvements

The potential test setup improvements fall into two categories: inexpensive and expensive.

The tank insulation could likely be improved. Using more homogeneous foam and better thermal radiation shielding would likely provide substantial heat leak

reductions. The lighting and pressurization systems need another iteration. The fiber optic lighting is not bright nor diffuse enough. Replacing it with a ring of surface mount LEDs with an integrated PCB heater and temperature control system would be fairly simple and inexpensive to design and make. This could be integrated into a new threaded pressure cap/view port. The tank could be machined perfectly spherical using the custom made brackets that were used to hold the tank halves during the flange facing. Though it would be difficult to do, triggering or controlling the motor controller with LabVIEW would streamline the testing process. Preloading the load cells more in compression and mixing their signals before being read by the DAQ would likely improve the quality of the force measurements.

A more expensive option for improving force measurements would be purchasing two new, smaller rated load, load cells. An even better (and more expensive) option would be to buy 3-4 triaxial load cells. By placing them at the corners of a frame holding the tank, these load cells could be used to obtain full 3-axis slosh forces and moments. Replacing the metallic tank with a pressurizable glass cryostat [10] would allow for better imaging and a lower heat load. While the foam insulation used is more characteristic of rockets than a cryostat, the convection currents from the high heat load may be affecting the slosh results and make determining the

effects of boiling difficult (see Section 6.1). Further fluid sensor development (see Section 4.3.5.4) should be considered expensive, mainly due the time involved.

4.4 Test Procedures

Two main types of tests were performed: forced sinusoidal excitation and damping. Fluid sensor calibration and static-boil off tests were also performed.

Deionized water was used for all water testing. The tank was incrementally filled with known volumes of water by measuring the water's mass using a scale with 0.5 g accuracy and assuming the density of water at 74 °F to be 997.5 kg/m^3. This proved to be more accurate than relying on the graduations of a graduated cylinder for volume measurement. Draining the tank was accomplished by siphoning through the vent port.

A chill-down process was used for LN_2 tests to prevent thermal shock. Small amounts of LN_2 were poured into the tank and allowed to boil off, after which the tank was filled and allowed to sit for a minimum of 30 min. The shower head device was also employed to help chill down the tank. Thermal equilibrium was checked via the thermocouples' readings during chill down. The volume of LN_2 in the tank was gauged using the internal ruler. Small fluid level changes were accomplished by letting the LN_2 boil-off, while large fluid level changes were accomplished with a fluid catch attached to a vacuum pump.

4.4.1 Damping Test Procedures

Damping tests were performed at 11 different volume fractions: 5, 10, 20, 30, 40, 50, 60, 70, 80, 90, and 95%. Each volume fraction was excited at the 1st mode resonant frequency (corresponding to that volume fraction) with a small amplitude for a previously determined number of cycles that resulted in the desired wave height. The excitation was then quick stopped and the slosh was allowed to decay while data was recorded. The tests were performed in this manner in an attempt to minimize the excitation of modes other than the first mode. Two different numbers of cycles were used to obtain a high and a low wave height, and each test repeated once, for a total of four damping tests at each volume fraction. The "high" wave height was determined by exciting for one less cycle than the number of cycles that would cause wave break up. The number of cycles for the "low" wave height was chosen such that the wave height would be about half that of the "high" wave height. The excitation frequency and amplitude were identical for water and LN_2. However, only the larger number of cycles were used for the LN_2 tests, but these were repeated as no boiling tests, which resulted in the same number of LN_2 tests as water tests. No boiling tests consist of a normal damping test, except the valve on the pressure relief system is shut for approximately 10-20 s during damping. This causes boiling to stop because the LN_2 follows its saturation curve while the pressure builds in the tank. The valve is then opened to vent the tank and boiling

resumes. The goal of the no boiling tests was to characterize the effect of boiling on damping factor.

Another set of tests were conducted at all volume fractions at a higher excitation amplitude in an attempt to obtain nonlinear damping data. The number of cycles was chosen so that splashing occurred before ceasing motion. The same procedures discussed above were followed.

The damping test procedures were modified for baffle testing. Only 30, 40, 50, 60, 70, and 80% volume fractions were tested since these were the ones most affected by the baffle. Two amplitude/number of cycle combinations were tested for each volume fraction, and each test was repeated once. All tests were identical for water and LN_2.

Data post-processing is done in MATLAB. All experimental data from a test is first imported and stored in a data structure. Because the actuator is triggered manually and not by LabVIEW, the start and end points of the test are found using a cosine fitting function to the LVDT position data. The end of excitation was considered the start of the damping test. Next, any non-lateral, e.g. off-axis or rotary, slosh are cut out; the lateral stop times were found prior to data processing by watching videos of every test, and the videos were generated by a custom MATLAB video creator script. The force, temperature, and fluid sensor data are detrended and then

filtered using MATLAB's non-casual `filtfilt` command with a 7th order Chebyshev Type-II IIR filter with a -50 dB gain at a 15 Hz cut-off frequency. Position and acceleration data are ignored for damping rate tests. The fluid sensor corrections mentioned in Section 4.3.5.4 are applied. A FFT-based algorithm is used to calculate the primary frequency of the damping slosh (which should be the 1st mode resonant frequency). Since the stage is not in motion during damping tests, the total forces measured by the load cells are the slosh forces.

Logarithmic decrement is calculated using two methods. Both methods start by finding the maximum-to-minimum force amplitude versus time. The total amplitude is used instead of just the maxima or minima because doing so seemed to reduce calculation noise slightly. The first method uses Eq. 3.3 directly to compute a logarithmic decrement for each cycle. The second method uses the MATLAB `fit` command to fit one or more exponentials of the form $Ae^{-b\Delta t}$ to the force amplitude versus time plot, where b is the logarithmic decrement. Method 1 usually results in a noisy curve that has to be smoothed; this is because small differences in the rate of change of either wave height or force amplitude are amplified by the cyclic ratio used in Eq. 3.3. Therefore, the exponential fitting method, while more computationally intensive, is preferred. All processed data is saved to the data structure binary file for that test.

Plotting scripts were written for each type of plot that loop through all relevant tests' data structures and pull the required parameters. These results are presented in Sections 6.1and 6.2. Test matrices are included in the Appendix.

4.4.2 Forced Sinusoidal Excitation Test Procedures

A forced sinusoidal excitation test consists of filling the tank to a specific volume fraction and exciting at approximately 15 frequency/amplitude combinations for approximately 60 s each, depending on frequency. Each test is repeated once. Nine volume fractions were planned, but time constraints meant that only two, 20 and 50%, were competed for water and four, 20, 50, 60, and 80%, were completed for LN_2. Frequencies were dependent on the fill level. The tank was excited at the first, second, and third asymmetric and symmetric mode frequencies, with various other frequencies spaced between these. The most common amplitude used was 2 mm. Some frequencies below the first mode frequency were excited with a 10 mm amplitude because 2 mm excitation did not cause much fluid motion. Four amplitudes were tested at the first mode resonant frequency: 0.466 mm, 0.934 mm, 1.866 mm, and 6 mm. The first three correspond to X0/D ratios from [27] and [4] so that direct comparisons could be made. Test procedures with the baffle were identical, except the 20% volume fraction was not tested as it was too low for the slosh waves to contact the baffle.

Post-processing for the forced sinusoidal data is similar to the damping data. Notable differences are that the excitation is now the focus of the data set, position and acceleration data are also detrended and filtered, and logarithmic decrement is not calculated. An additional cosine waveform fit to the filtered position data is performed to determine the actual excited amplitude and controller error. As mentioned earlier, the maximum excitation amplitude error was 4%, with an average of 1%. Since the tank was constantly in motion, the force data collected includes the inertia of the tank and frame and any additional forces acting on them. These forces have to be subtracted from the total (measured) forces to derive the slosh forces. Empty tank tests at all frequency/amplitude combinations were performed, and the forces from those tests are processed and filtered in a similar manner to the fluid tests. A cycle-averaged empty force is computed and a complete cycle-averaged empty force waveform is constructed for each fluid test using a custom algorithm. This method is preferable to subtracting structural mass times acceleration from the total forces because it only relies on one type of sensor instead of three (scale and accelerometer are the additional two), and it corrects for any additional forces, e.g. LVDT spring force, wire pull force, etc. After processing, all data is stored in the test's data structure binary file.

Plotting scripts were written for each type of plot that loop through all relevant tests' data structures and pull the required parameters. These results are presented in Section 4.6.5 and 6.3. Test matrices are included in the Appendix.

4.4.3 Determination of Resonant Frequencies

Before conducting and "real" tests, an attempt was made to experimentally verify the theoretical 1st, 2nd, and 3rd mode resonant frequencies using water. Two methods were used: free damping and continuous forced excitation. The second method involved tuning the excitation frequency to obtain the maximum force response. After much experimentation, it was determined that this method could not be more precise than about 0.05 Hz, so Method 1 was favored over Method 2. In Method 1, the damping test procedures for high amplitude were followed with a few modifications. The force decay waveform was split into three ranges, and the primary frequencies were computed (via FFT) for each range. These were compared to the frequencies calculated from the whole waveform. For every fill level, the 1st mode frequency increased as the force decayed. The 1st mode frequency computed from the whole waveform, which was always within ±0.05 Hz of the high and low ranges, agreed well with the theory. For three volume fractions, the experiments predicted frequencies higher than the theory by greater than 0.01 Hz (50, 90, and 95%), so the experimental 1st mode frequency (computed from the whole waveform) was chosen over the theoretical value for "real" testing at these

volume fractions. The theoretical values were used in real tests for all other volume fractions. The reason the 50% experimental 1st mode is at a slightly higher frequency than theory is due to the cylindrical section around the middle of the tank from flange weld deformation. The diameter in this part of the tank is slightly smaller than it would be in a perfect sphere, which causes the slight increase in 1st mode frequency. The reason the 90 and 95% experimental 1st mode frequencies are slightly higher than theory is likely because it was not possible to excite to as high of an amplitude due to wall curvature promoting wave breakup, and as mentioned earlier, lower amplitude slosh results in a slightly higher mode frequency.

Generally, the 2nd and 3rd modes were not visible with this method due to them not being strongly excited, though occasionally a small peak was seen in the FFT around where the 2nd or 3rd mode should be.

The 1st mode frequency was also computed during all experimental and CFD damping tests (see Section 6.1).

4.4.4 Fluid Sensor Calibration Procedures

Calibration tests were performed before, during, and after each round of testing. Each test consisted of recording the fluid level (known volume for water, ruler reading for LN_2) and collecting fluid sensor data at 200 Hz for at least 15 s. This data was time averaged to obtain a single voltage versus arc mm point. 20-50 of

these points were obtained for each set of data and used to create a linear fit and the calibration coefficients.

4.5 Uncertainty

Many sources of error have been discussed in the previous sections. Some of these will elaborated on here and a few more will be mentioned. Note that a rigorous uncertainty analysis has not been performed for any of the sensors or results, primarily due to time, but also due to impracticality for some cases.

Shrinkage of the aluminum tank's radius at LN2 temperature was calculated to be about 1 mm. Observations of the movement of the tank's brackets (the screws for which are not fully tightened to the frame until after chill-down) show somewhere between 0.5 mm and 1 mm of movement, which corresponds to a volume loss of approximately 140-280 mL (1-2%). No corrections have been made for this change in volume.

The tank was filled with water by filling a graduated cylinder with an approximate volume of water, placing it on a scale with 0.5 g resolution, adjusting the amount of water until the mass was correct given a density of water of 997.5 kg/m^3 at 74 °F, pouring it in the tank, and then repeating. Thus, the volume uncertainty of water in the tank increases with fill level proportional to the number of fill events. Assuming each fill event was off by 1 g, the density was off by a maximum of 1

kg/m^3, and 20 fill events, the maximum volume of water error would be approximately 20 mL. Because the total tank volume was measured in a similar manner, this is also approximately the uncertainty of the volume of the tank.

Because the volume of LN_2 was gauged using the internal ruler, the LN_2 volume uncertainty is significantly higher than that of water. The internal ruler was not located perfectly along the circumference, and it was on a slightly smaller radius than the outer wall of the tank because it was attached to the fluid sensor. Using the aforementioned water filling method and assuming a perfect sphere for geometric relations, the linear function to convert from ruler arc mm to true arc mm was found with an R^2=0.99993. Thus, the volume error due to the ruler arc mm to true arc mm conversion is approximately that of the volume of the tank, or 20 mL. Because the volume is gauged with the ruler, and the volume in the tank is nonlinear with height, the error will be worst at the largest surface area location (assuming constant ruler reading error), which is at the 50% level. For the majority of the tank, most of the error in reading the ruler with LN_2 comes from the natural convection currents along the wall obscuring the exact fluid-gas interface. The convection currents caused ripples that ranged from approximately ±3 mm near the bottom of the tank to ±5 mm near the top of the tank. Assuming ±4 mm at the 50% level (worst case), that equates to approximately ±270 mL (±2%). The error in reading the ruler in the top 10% of volume in the tank was higher because seeing

the ruler was more difficult. A USB snake camera was used to read the ruler at all fill levels, but it could not see the top ~100 mm of the ruler without using a mirror attachment. The mirror attachment tended to obscure the markings on the ruler more, so the error for the 90 and 95% volume fraction tests is likely closer to ±10 mm. At the 90% level (worst case), this equates to approximately -375/+320 mL of error. None of the above accounts for the approximately 140 to 280 mL of volume error due to tank shrinkage mentioned earlier. Total LN_2 volume error as a function of fill level has not been estimated, but given the above discussion, it is unlikely to be worse than about 4% for any fill level (~600 mL for a full tank). As discussed in Section 4.3.7, a better (and more expensive) force sensor measurement setup would allow for the measurement of triaxial forces. A convenient result of this is that fluid mass gauging could be accomplished through measurements of the vertical axis force, which would significantly reduce volume error.

The load cell discussion in Section 4.3.4.2 mentioned accuracy and nonlinearity problems, and these will be elaborated on here. During post-processing, it was determined that the load cells were not capable of accurately measuring forces within 1 N of no load during motion. While the exact reason for this is unclear, it is likely due to a nonlinear deadband region. The nonlinearity manifests as a non-uniform distribution of force between the two load cells and a nonlinear delay with respect to the LVDT and accelerometer. At high forces (>2 N), the delay is

approximately 4-6 ms, which is close to the 4 ms calculated for the 4 pole filter present in the SCXI-1520 load cell module (see Section 4.3.4.1). This would not be a problem if the delay was constant for all forces. Because the slosh forces are calculated by subtracting the empty tank forces (see Section 4.4.2), if the delay was the same for both, having a delay would not matter. The force or the motion waveforms could simply be time shifted a few ms to compensate. However, at low forces (<1 N), this delay increases to 100's of ms in a non-predictable manner. Attempts to compensate for this error have failed, and so any *measured* loads (not slosh forces) of < 1 N should not be trusted, and any measured loads between 1-2 N should probably be assumed to have error of the same order of the measurement (~1 N). Fortunately, measuring low forces are not the focus of this study, and adding fluid increases the mass, which increases the loads and pushes most of the cases into the constant delay range. Even if the slosh forces are near 1 N in amplitude, the total forces on the load cells may be high, e.g. higher frequency cases, making the error on the slosh forces low. To lend support to this theory, for most forced excitation tests, time shifting the empty mass * acceleration to match up with the cycle averaged empty tank forces, then computing the slosh forces by subtracting either from the total forces, tends to result in similar slosh forces waveforms. However, for low force cases, the slosh force waveforms calculated by the two methods do not generally agree well, though the average amplitude seems to be fairly similar. Note that the prior comparisons were purely qualitative

assessments from plots. The static error for each load cell was determined by the root-sum-square method of the errors in the datasheet to be ±0.2 N at the maximum load measured (not including DAQ errors). Though the dynamic error for the whole force measurement system has not been calculated, it is likely closer to ±1 N given the above discussion.

The LVDT was calibrated while connected in the final instrumentation configuration using 10 points over 1 in with a micrometer that has 0.00005 in precision. A few seconds of data at each of the points was collected and averaged. The resulting voltage to mm conversion factor was calculated in Excel via linear regression and placed in the LabVIEW VI. While error bounds for static readings might be possible to obtain through repeated measurements using the micrometer, the dynamic error is too impractical to obtain. Examination of the LVDT data shows sufficient precision for all tested motions. In fact, it was capable of measuring the load cell deflections (of order 1 μm) after excitation during damping tests.

A rigorous uncertainty analysis of the accelerometer could not be accomplished. While the manual and calibration certificates were found, the exact model type and data sheet for the 15 year old sensor could not be found. The accelerometer was calibrated and zeroed using gravity as a reference, then a factor of 9.80665 m/s^2 was applied in the LabVIEW VI to convert the sensor output of g's to m/s^2. While

error bounds for static readings might be possible to obtain through repeated gravity measurements, the dynamic error is too impractical to obtain. Examination of the accelerometer data after low-pass filtering shows sufficient precision for all tested motions. Note that the accelerometer data was not used in the calculation of any relevant parameters.

Fluid sensor error sources were thoroughly discussed in Section 4.3.5. Determining an overall dynamic uncertainty for the sensor is impractical until a more commercializable design is developed. As stated earlier, the best estimate of the accuracy for the sensor is ±10 mm for LN_2 and ±5 mm for water, but this is based on qualitative observation. The higher error for the LN_2 is mainly because the ruler was used to gauge the fluid volume for calibration (see the volume discussion earlier in this section).

Because the SCXI channels were calibrated and an 18 bit ADC was used, the dominant thermocouple error is likely the inherent error of the thermocouples, which is ±2 °C.

Because of the dynamic nature of many of the quantities required for calculating the relevant parameters, e.g. damping factor, error bounds (via a rigorous uncertainty analysis) for these parameters have not been estimated. The best approach for estimating a confidence interval for these parameters would be to

repeat each test many times and perform a statistical analysis on the results. Each test for this project was repeated once, but three or more repeats are likely necessary. Unfortunately, there was not enough time to perform more repetitions.

4.6 Results

The results and discussion in this section are specific to the experiment portion of this project. More experimental results are presented in Chapter 6.

4.6.1 Static Boil-off and Heat Leaks

Between LN_2 baffle damping fluid levels, static boil-off rates were measured by recording the fluid level on the internal ruler, setting a stop watch for 20 min, then recording the fluid level on the internal ruler again. Table 2 summarizes the results of these tests.

Table 2. Static Boil-Off Test Results

Arc height start [m]	Arc height end [m]	Boil-off rate [kg/h]
0.293	0.284	1.25
0.275	0.266	1.47
0.25	0.242	1.45
0.228	0.22	1.38
0.206	0.2	0.95

Typically, higher fill levels have a higher heat leak due to a larger average temperature difference over the area of the tank. The first test in the table was done immediately after a no boiling damping test; these tests utilize the showerhead

device to drip LN_2 around the outside of the tank walls to lower the heat leak into the tank. The lower boil-off rate is likely due to the tank walls not having returned to thermal equilibrium yet. While the effects of the baffle have not been quantified, it is likely that the baffle increases the heat leak some by drawing in heat from the tank flanges.

Using the boil-off rates and thermocouple data, some rough estimates of heating and the relative contribution of some heat leak paths can be made. Using the heat of vaporization of LN_2 and a boil-off rate of 1.4 kg/h, the total heat leak into the tank is approximately 77 W. Using the 1D steady heat conduction equation, the thermal conductivity for low density polyurethane foam at a reduced temperature, and the geometry of the insulation, the heat leak due to conduction through the insulation is approximately 41 W. The heat leak through the polycarbonate tank brackets was calculated to be approximately 2 W. Conduction through the optical fibers will be less than the polycarbonate brackets due to a similar conductivity and lower area. That leaves approximately 34 W of heat leak; insulation imperfections and radiative heat transfer likely accounts for most of that.

Future plans include using these tests, along with the temperature data, to validate a NASA Generalized Fluid System Simulation Program (GFSSP) static boil-off model of the tank.

4.6.2 Thermocouples

The thermoprobes located above, but close to, the static fluid level managed to register slosh events during LN_2 tests. These are seen as a sudden drop in temperature, and then temperature oscillations at the fluid frequencies present in the tests, e.g. first mode for damping tests. In fact, FFTs of some tests indicated the second mode was also being registered.

In addition to registering slosh events, the thermoprobes and exterior-wall thermocouples also gathered data relevant to studying stratification and de-stratification. While usually not seen in tanks this small, ullage and propellant stratification was measurable in this case due to the high heat leak. Initial slosh waves caused the ullage temperatures to drop significantly, and a pressure spike was observed via a sudden increase in the vented N_2 plume in most high wave amplitude tests. Ullage pressure collapse was not observed, likely due to the high heat leak. Since studying stratification was not an objective of this project (and the CFD was isothermal), no further work was done in this area, though the data is available for future research.

4.6.3 Damping

All experimental damping results and discussion are presented in Chapter 6.

4.6.4 Forced Excitation

The majority of the no baffle experimental forced sinusoidal excitation results and discussions are presented in Chapter 6.

Rotary slosh, i.e. slosh rotating about the vertical tank axis, was observed for every fill level during forced excitation testing. In fact, the highest forces recorded were during 1st rotary mode sloshing. Note that tank was only excited laterally, yet rotational modes developed. This phenomena has been seen in past experiments [4], but has not been heavily investigated. One of the theories for how this occurs is as follows: The chaotic motion from a breaking wave re-entering the bulk fluid causes an off-axis force and resulting fluid motion. A component of the splash-induced motion is re-directed by the wall giving an initial rotation. Since the rotational slosh mode in spherical tanks is less damped than the lateral slosh mode (observed in these experiments), and the rotational slosh first mode frequency is near that of the lateral slosh first mode [4], the lateral sloshing mode tends to transfer energy to the rotational mode and decay quickly. If the forcing frequency is not exactly that of the rotational mode's resonant frequency, lateral and rotational modes may interchange energy, resulting in a pattern of lateral (often off-axis) slosh, mixed with rotational slosh. The off-axis angle and rotation direction seemed to be sensitive to initial conditions and frequency. The speed at which these patterns developed and decayed was dependent on amplitude, with higher amplitudes causing faster evolution. This quasi-rotational behavior was observed in

many tests near the 1st, 2nd, and 3rd lateral asymmetric modes. Careful tuning of the frequency and amplitude sometimes resulted in stable rotation of the 1st, 2nd, and 3rd rotary modes for the tank, and the following table summarizes these results. Note that these are not the only cases where rotation was observed, but the only cases where (at least somewhat) stable rotation was observed. Discovering these rotary modes was unexpected and not an objective of this project, but the potential for future research was clear, so some time was spent trying to find them.

Table 3. Rotary Modes

Fluid	Vol. %	Mode	f [Hz]	X_0 [mm]	Comments
W	20	1	1.47	2	Stable
W	20	1	1.49	3	Stable
W	20	2	3.02	2	Stable
W	20	3	4	2	Stable
W	50	1	1.67	2	Stable
W	50	1	1.71	3	Stable
W	50	2	3.1	2	Stable
W	50	3	3.9	1	Stable
LN2	20	1	1.49	3	Hard to excite, requires initial rotation
LN2	20	2	3	2	Hard to excite. Devolves into “weird” mode (discussed below)
LN2	50	1	1.67	3	Stable
LN2	80	1	2	2	Stable
LN2	80	2	3.18	2	Starts splashing, maybe slightly lower amplitude needed

Some modes seemed to have ranges of amplitudes and frequencies that would result in stable rotation. The 2nd and 3rd rotary modes for 50%, and 3rd rotary mode for 20% were not successfully excited in LN_2 tests. No stable rotary modes were

excited for 60% LN_2. In general, it was more difficult to excite rotation with LN_2 than with water. This is counter-intuitive because one would think that the randomness of the turbulent convection currents would encourage some initial rotation, but this is not the case.

No analytical models of rotational slosh were developed for this project, though they do exist. [4] [6]

Two CFD cases, one of which is presented in 6.3 compared to an experiment, showed rotation naturally develop from lateral excitation. "Naturally" here means that no initial rotation or off-axis motion was applied. Small asymmetries in the mesh or error from the solution scheme likely caused the initial asymmetry required for the rotational mode to develop. The author is unaware of any successful attempts to excite a rotary slosh mode in a tank with pure lateral excitation in CFD, though it is likely that some researchers or CFD industry professionals have observed this before.

In addition to rotational modes, some "weird" modes were seen at excitation frequencies around and above the 2^{nd} lateral mode after a brief period of lateral sloshing. These "weird" modes are characterized by oscillating patterns that look like they might be combinations of different modes. Sometimes the patterns evolve over time, and sometimes they devolve into chaotic motion. As long as the motion

in these cases was not obviously rotational, these regions were not cut out of the data for computation of the force parameters.

4.6.5 Forced Excitation with a Baffle

No CFD cases were run for forced excitation with a baffle due to time constraints, so all of the baffle forced excitation experimental data is presented and discussed in this section. Over 100 forced excitation baffle tests were conducted. Since no analytical or CFD is available for comparison, time domain plots do not offer much interesting information, so they have been excluded here.

The following three figures are plots of the non-dimensional slosh force parameter, $F_{max}/\rho g D^3$, versus the non-dimensional frequency parameter, $\omega\sqrt{R/g}$, for three volume fractions with and without the baffle. The theoretical unrestricted 1st and 2nd modes are shown as dashed vertical lines. These plots show the effect the baffle has on the frequency response of the tank.

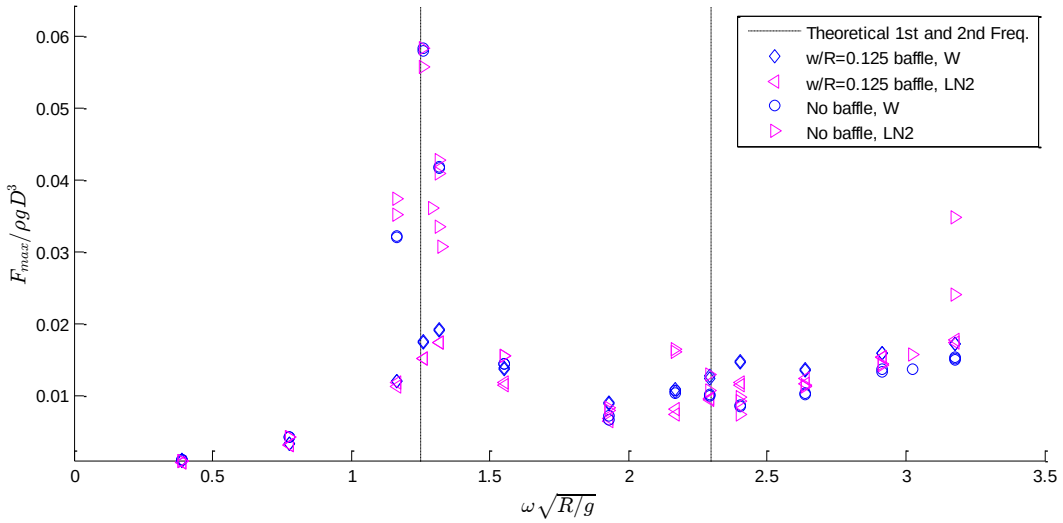

Figure 13. Slosh Force Parameter vs. Frequency Parameter for 50% Volume Fraction

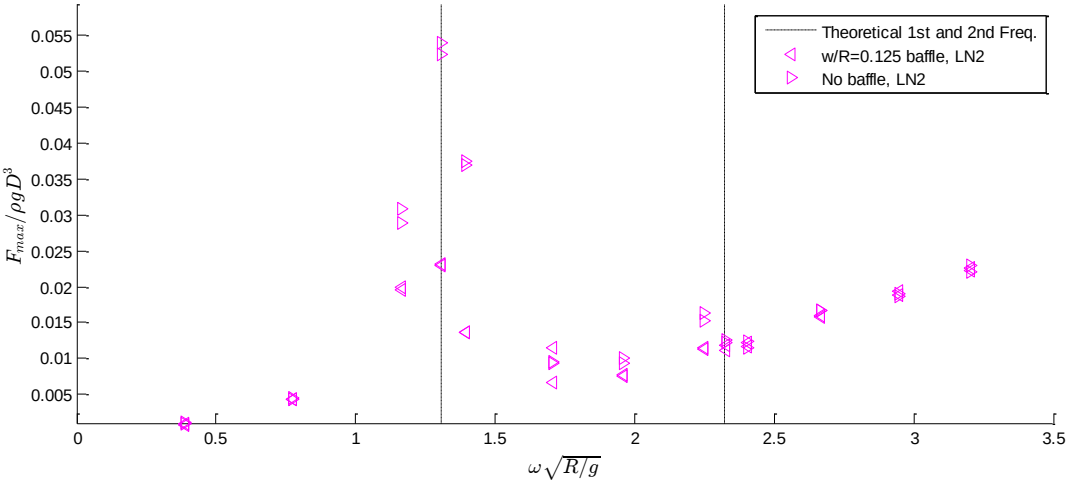

Figure 14. Slosh Force Parameter vs. Frequency Parameter for 60% Volume Fraction

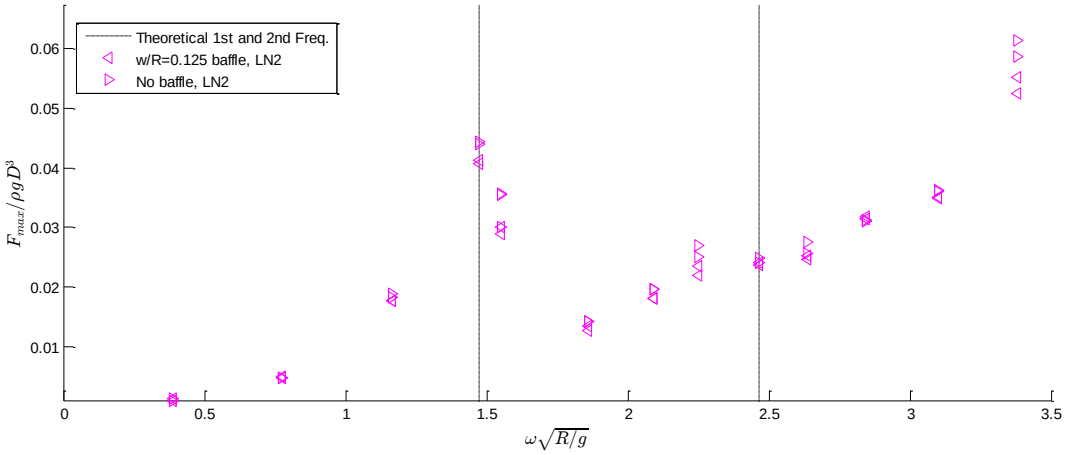

Figure 15. Slosh Force Parameter vs. Frequency Parameter for 80% Volume Fraction

Water data is plotted against LN_2 data for 50% in Figure 13, but not for 60% and 80% because water tests were not conducted at those fill levels. The water and LN_2 data agrees well, usually within 10%. The largest discrepancy between water and LN_2 is the no baffle LN_2 points at the highest frequency; a large amplitude "weird" mode developed during those tests that was suppressed with the baffle. The baffle suppresses the slosh forces around the first mode resonant frequency by a factor of 3. Also worth noting in Figure 13 are the peaks that occur just after the 1st and 2nd mode resonant frequencies in the baffle data. When the fluid level is at the level of the baffle, the baffle tends to act as a restriction in the diameter of the tank, which pushes the resonant frequency higher (see Figure 29). Comparing Figures 13-15 shows that the baffle becomes less effective as depth and frequency increase. The former makes intuitive sense; the velocity of the fluid drops rapidly with depth in a sloshing tank, so the baffle is not providing as much drag. The fact that baffles are

maximally effective when they are near the free surface is the reason that multiple baffles are often used in tanks [4]. The reason that ring baffles are less effective at higher frequencies is less clear. The most likely cause is that the higher frequency cases have lower wave amplitudes (compared to near-resonance cases), and so the baffle cannot attenuate the slosh waves as much, resulting in less of an effect.

Only one of the resonant frequency tests is presented in Figures 13-15, specifically the 1.866 mm excitation tests. This is because it is the closest to the most common excitation amplitude of 2 mm, and adding the other three resonant frequency tests would clutter the graphs. Even though 2 mm was the most common excitation amplitude, a few of the tests were done at different amplitudes (see Appendix). An amplitude correction factor of X_0/2mm was applied to the force parameter for these cases. This is not necessary for the other form of the force parameter, $F_{max}/\rho g D^2 X_0$, as it is non-dimensionalized by the excitation amplitude. The form of the force parameter in the figures in this section was used because it allows for easier comparison to Ref. [26]. However, the X_0/D's in [26] are not the same as the ones used in this project, and so a direct comparison to past force parameter versus frequency parameter data is not possible.

The following three figures are plots of the non-dimensional 1st mode slosh force parameter, $F_s/\rho g D^3$, versus the non-dimensional excitation parameter, X_0/D, for three volume fractions. The difference between the slosh force parameter in Figures

15-17, and the one in Figures 12-14, is that this one is calculated only from the first mode resonant frequency tests. These plots depict the effect of excitation amplitude and the baffle on the maximum slosh forces.

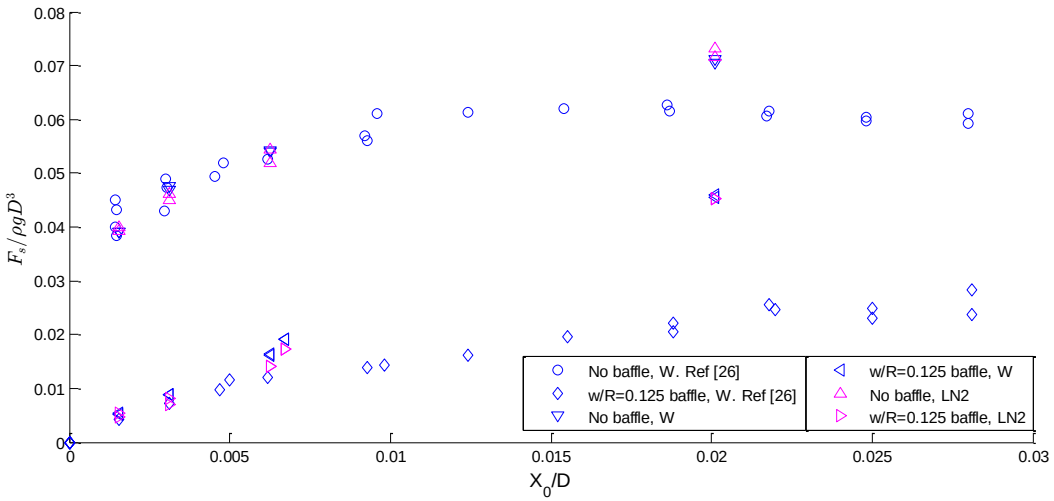

Figure 16. 1st Mode Slosh Force Parameter vs. Excitation Amplitude Parameter for 50% VF

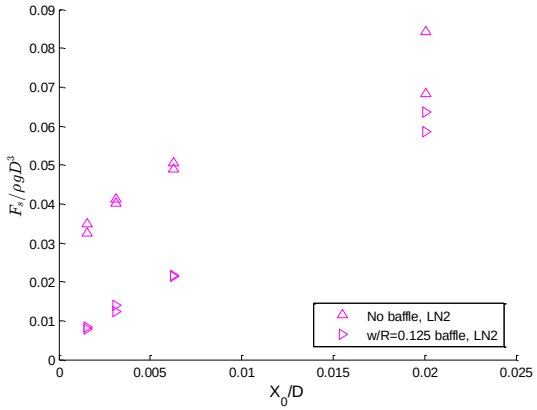

Figure 17. 1st Mode Slosh Force Parameter vs. Excitation Amplitude Parameter for 60% VF

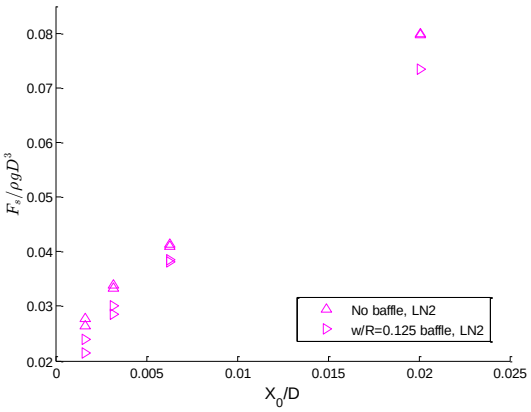

Figure 18. 1st Mode Slosh Force Parameter vs. Excitation Amplitude Parameter for 80% VF

Figure 16 shows experimental water and LN_2 data with and without a baffle versus water data with and without a baffle from [26]. The agreement between past and present water results and LN_2 results is usually within 10% except for the largest amplitude cases, which correspond to 6 mm excitation. This discrepancy is due to a difference in the way the tests were performed. The forced excitation tests in [26] were stopped before significant wave-break up occurred, and the first force peak after motion stop was used to calculate the force parameter. The forced excitation tests in this project were forced continuously regardless of splashing, and the highest recorded force (lateral slosh only) was used to calculate the force parameter for each test. This is also the reason the "leveling off" trend seen in the past data in Figure 16 is not seen in the present data. Another conclusion that can be drawn is that this ring baffle is less effective with high amplitude splashing slosh. A

hypothesis for why this is that the baffle is simply being overwhelmed; tests with a higher w/R baffle could be conducted to test this hypothesis. Comparing Figures 15-17, it is again clear that the baffle becomes less effective with depth: the attenuation decreases from a factor of approximately five at 50% to less than two at 80%.

A key conclusion that can be drawn from the forced excitation baffle testing is that, if non-dimensional slosh forces for fluid levels near the baffle are the only concern, water can be used as an analog for LN_2. This makes sense physically because the majority of the damping in a baffled tank comes from the baffle instead of the viscous boundary layer, so a difference in viscosity is not as important. However, if thermal effects, e.g. de-stratification and pressure spikes, are of concern, forced excitation baffle testing should be conducted with a cryogen.

Note that all tests were repeated once and results from both are plotted. If only one symbol is visible for any given case, it is because the results are so similar that the symbols overlap.

While the above plots and discussion pertained to lateral slosh, the baffle tended to be effective in suppressing rotational slosh, too. 2^{nd} and 3^{rd} rotary modes (pure rotation) were observed for 50% LN_2 at 3.4 Hz, 2 mm and 4.1 Hz, 2mm respectively. These are higher frequencies than the 2^{nd} and 3^{rd} rotary modes for

50% discovered for water in the no baffle tank because the baffle creates a smaller effective diameter. Non-pure rotation was observed in a few other tests.

Chapter 5 Numerical

5.1 CFD

5.1.1 Software and Environment

All CFD simulations were performed using STAR-CCM+ v9 and v10 on hardware at NASA KSC.

5.1.2 Meshes and Settings

The tank is modeled as closed, perfect sphere except for a 15 mm flattened cylindrical section around the center corresponding to the flange weld-deformed region. No other imperfections were modeled, e.g. non-constant radii, fluid sensor, thermoprobes. Two primary meshes were used, and their cross-sections are depicted in the following figure:

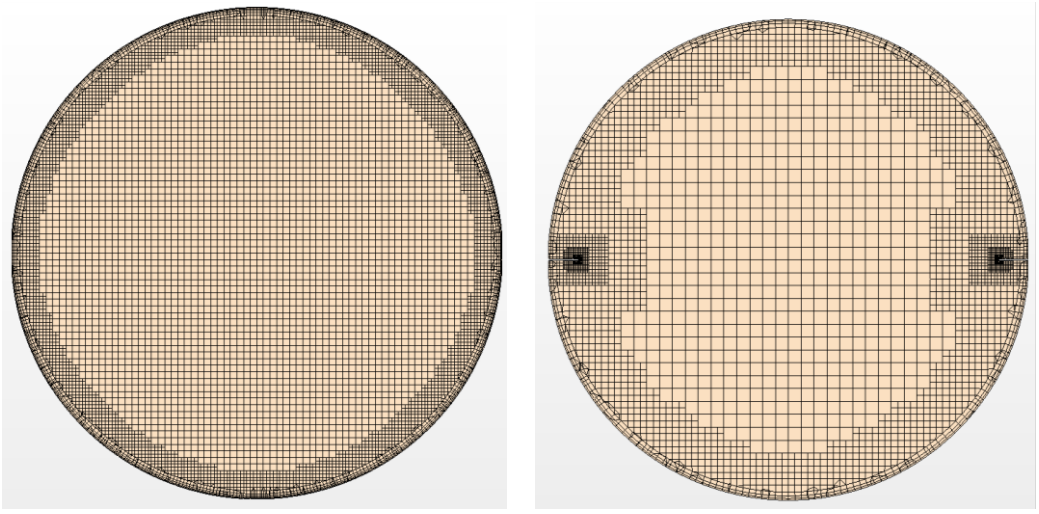

Figure 19. Normal Mesh (*left*), Baffle Mesh (*right*)

All meshes are hexahedral dominant with prism layer cells along the wall and some polyhedral connecting cells. The first mesh is approximately 1M cells and used for most of the non-baffle simulations. The prism layer thickness was set by an estimate of the boundary layer thickness assuming laminar flow, and as many layers as would stay under 1M cells were used in an attempt to better resolve the boundary layer. The second mesh is approximately 740K cells and is heavily refined around the baffle, while other regions are coarsened relative to the non-baffle mesh. This was done because the majority of the damping for the baffle simulations is from the baffle, while the majority of the damping for the non-baffle simulations is from the viscous boundary layer. An additional 1M cell mesh (see Figure 20) was made heavily refined around the 60% volume fraction level and coarsened elsewhere. This was used to test the effects of surface tension on low amplitude (<10 mm wave height) water damping, which is discussed in Section 6.1.

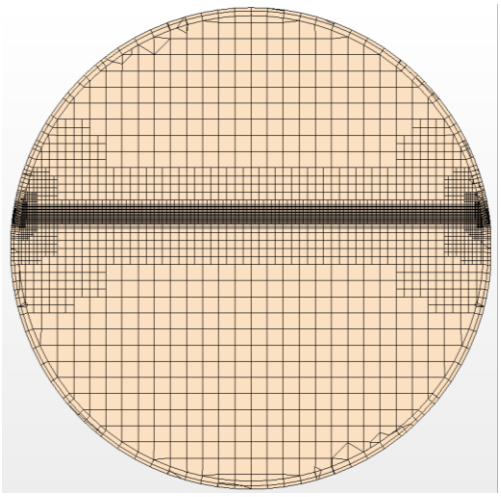

Figure 20. Mesh Refined around 60% Volume Fraction

A set of custom-written JAVA macros automated the case building process. Volume fraction was initialized with a field function. A set of field functions were written to emulate the fluid sensor in the real tank in order to measure fluid wall height as a function of time. Because STAR-CCM+ does not have LN_2 as one of its fluids, properties for LN_2 from NIST data were placed in a custom material library. While the gas phase plays little roll in slosh dynamics, the N_2 properties for all LN_2 cases were set corresponding to 1 atm and -150 °C.

Motion was implemented using a field function and user-defined vertex motion. Two field functions were tried. One imported a table of the filtered experimental position data. Tiny slope changes in the position data caused large force oscillations in the CFD. It was reasoned that the effects of the imperfections in the position profile should be small since no large force oscillations were observed in the experiments. Thus, a second field function was implemented and ultimately used

that calculated a pure cosine position profile based on frequency, amplitude, and number of cycles.

Solution histories were not saved due to the massive (50 Gb+) resulting files. Instead, images of the fluid free surface from a side, top, and isometric view were saved every 0.025 s. Note that no image-to-camera frame comparisons will be made in this thesis. This is because the exact lighting, transparency, and perspective could not be recreated in STAR-CCM+, and attempts to undistort the pictures taken with the fisheye lens were unsatisfactory (see Section 4.3.4.5). Slow motion video is the best method in which to qualitatively compare the fluid surface of the experiments and CFD because the dominant dynamic flow features can be observed. The data recorded during simulation included tri-axial slosh forces, tri-axial moments, tri-axial center of mass displacement, wall height, average CFL number, and maximum CFL number. A macro automated the data exporting process.

The following settings were used for all simulations: implicit unsteady with 2nd order accurate time and space formulation, multiphase segregated volume-of-fluid (VOF), laminar, constant density fluids. The number of iterations per time step was set such that all of the residuals level out.

A grid and time step independence study was started. The mesh was refined and time steps reduced until the cases became infeasible to run within a few days. At that point, neither grid nor time step independence could be established. The aforementioned meshes and a time step of 0.001 s were used for most of the simulations presented in this paper with the hope that the experimental results would agree well.

5.1.3 Simulation Procedures

In general, the simulations followed a similar procedure to their corresponding experiments. In other words, the same volume fractions, frequencies, amplitudes, number of cycles, etc. in the experimental test matrices were used as inputs for the CFD. However, all CFD cases were run for significantly less time than their experimental counterparts. In general, 8-15 post-excitation oscillations were used per damping case, and forced sinusoidal excitation cases were run for about 10-15 s.

Once the data files were generated, they were post-processed using MATLAB scripts similar to those used for the experiments. Because the CFD was not subject to real world noise and problems, the CFD post-processing scripts were less complicated.

5.1.4 Results

All CFD results are presented in Chapter 6 for comparison to experimental and analytical results.

5.1.5 Potential Improvements

Before comparing the CFD results to the experimental results, it is worth noting some potential improvements to the CFD methodology presented here.

First, the fluid sensor in the experiment and the fluid sensor emulating function were on opposite sides of the tank relative to initial excitation direction. This mistake was not noticed until the majority of the CFD cases had been completed. The effects of this can be seen in the time domain plots of wall height; the wall height for the CFD looks 180 degrees out of phase. While this does affect the time domain comparisons, it should not affect any of the calculated parameter comparisons, including WHDLDs. This mistake was corrected for a few of the later cases by rewriting the field functions, which were also simplified by using a velocity reference frame motion instead of a user-defined vertex motion.

Judging by the intermediate results of the mesh and time independence study, neither grid nor time step independence has been obtained, though the simulations seem to be more dependent on the latter for these meshes. Thus, it is likely that greater improvements to accuracy could be achieved by decreasing time step than increasing mesh refinement for the same computation time. A time step of 0.0005 s

was used for a few of the CFD cases to try to reduce error with inconclusive results. Due to the oscillatory nature of fluid slosh, an adaptive time stepping scheme could be beneficial for improving accuracy and decreasing computation time. Adaptive time stepping based on a constant average or maximum CFL number works by increasing the time step when the fluid speed is low and decreasing time step when the fluid speed is high. STAR-CCM+ does not natively support adaptive time stepping, though it can be added as a field function or macro.

Creating a mesh similar to Figure 20 for every volume fraction would likely increase accuracy. This is because the majority of the domain's damping and physical phenomena are happening in a narrow band around the gas-fluid interface; the fluid far below the interface and the majority of the gas phase only have a minor effect on the slosh dynamics. However, high amplitude slosh would require the refinement band to be large, resulting in meshes too large to be practical. This is part of the reason one mesh (one for non-baffle and one for baffle) was used for most cases. Another reason a single mesh was used for most cases was to eliminate the mesh as a possible reason for a discrepancy between fill levels. Instead of creating a fixed, wide band for high amplitude slosh, it would be better to move the band with the sloshing motion, i.e. refine the mesh only where the fluid dynamics are significant. This is the idea behind adaptive mesh refinement. Unfortunately,

adaptive mesh refinement is not a feature in STAR-CCM+, and adding it (if possible) would be difficult.

Chapter 6 Comparison of Results

6.1 Damping

The experimental, numerical, and empirical correlation unrestricted damping data will be presented in this section. Approximately 140 experimental damping tests were run. Seven CFD damping cases were completed for water, and twelve CFD damping cases were completed for LN_2. Multiple CFD cases at the same fill level usually represent different initial wave heights. No CFD cases corresponding to nonlinear experiments were completed.

The following two plots depict experimental and CFD first mode frequencies computed by FFT of force decay waveforms for water and LN_2. The theory for the first mode is also included in the plots.

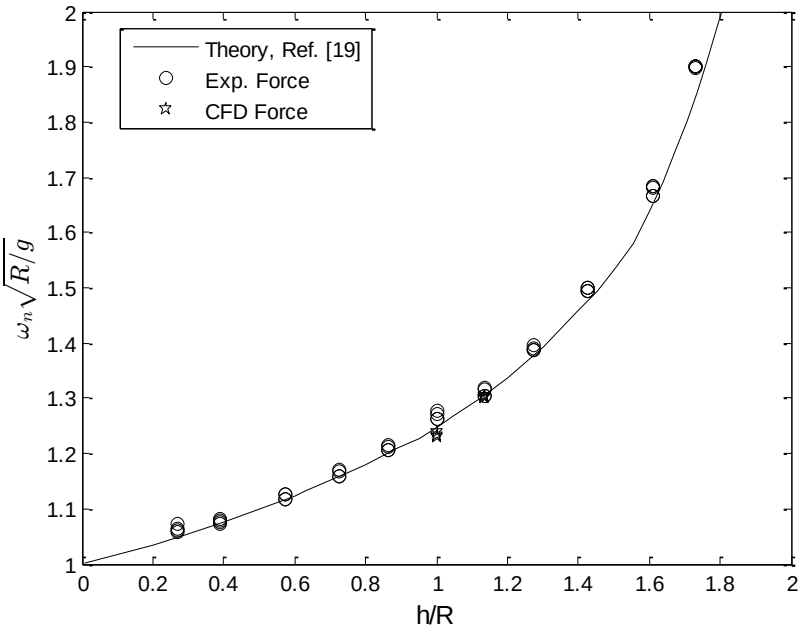

Figure 21. 1st Mode Frequency Parameter vs. Fill Fraction for Water

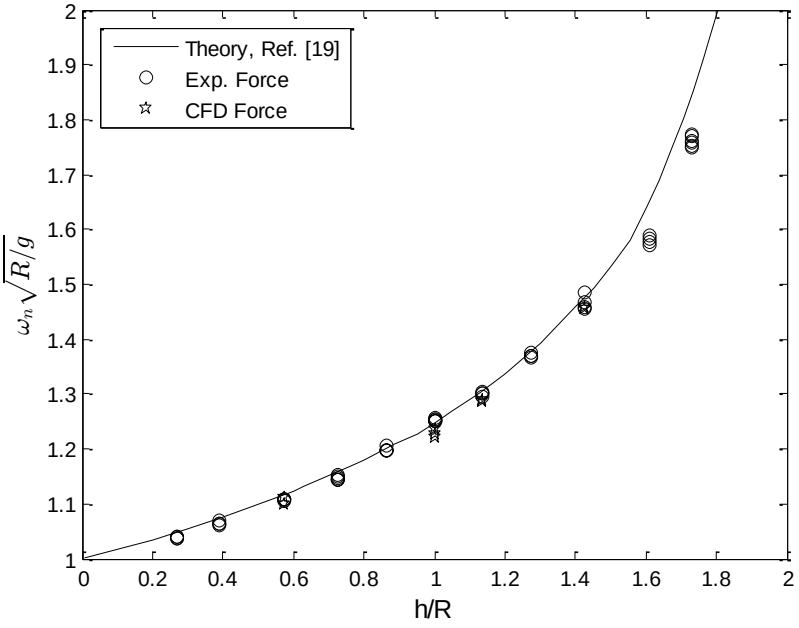

Figure 22. 1st Mode Frequency Parameter vs. Fill Fraction for LN_2

Overall, agreement between theory, experiment, and CFD for the first mode frequencies for water and LN_2 are usually within 2%. Two minor discrepancies in Figure 21 need to be addressed. At the 50% fill level, the experimental results are slightly above the theoretical; the reason for this is an effective reduction the tank diameter there (see Section 4.4.3). Interestingly, the CFD has the opposite trend because no low amplitude CFD cases were done at a fill level of 50%, and as discussed in Section 4.4.3, higher amplitude slosh tends to have a slightly lower frequency. "Slightly" is defined here as up to -0.05 Hz (again, see Section 4.4.3), which is -0.039 in frequency parameter terms; the CFD results are within this range. The second discrepancy is that 70-95% volume fractions' frequencies are all about 3% above the theoretical frequency; it is unclear why this is the case. The same discrepancies at 50% with water are present in Figure 22 for the same reasons. The largest differences between the theoretical and experimental frequencies are at 90 and 95%. These were the fill levels that had a higher volume gauging error (see Section 4.5). Assuming the volume in the experiments was low, horizontal lines can be drawn from the middles of the 90 and 95% clusters of points over to the theoretical line. Comparing these fill fractions yields differences in volumes of about 365 mL and 260 mL for 90 and 95% respectively. In other words, the real volume fractions for those fill levels were likely around 87.4% and 93.1% respectively. Note that these errors are within the uncertainty for these fill levels mentioned in Section 4.5. Most of the experimental and CFD cases lie below the

theory line, and the reason for this is not clear. One possibility is that the fluid level was consistently low for all cases, and the differences are within the estimated volume uncertainty. It is also possible that a physical reason may be causing this trend, perhaps some sort of interaction between the natural convection boundary layer and the slosh.

According to linear slosh theory, the rate of decay of slosh force and wave height should be a perfect exponential corresponding to a constant logarithmic decrement for all wave heights. Most sources state that the damping factor should not be dependent on wave height, but give little support to this statement [4] [5] [24]. No past research was found that attempted to find a relationship between wave height and damping factor for spherical tank slosh. As will be shown in the following figures, damping tests from this project show a strong relationship between wave height and logarithmic decrement for water.

A good metric for plotting the logarithmic decrement had to be found, since plotting it versus time makes comparing different tests difficult. Plotting logarithmic decrement versus slosh force does not make much sense either, because the slosh forces are dependent on fluid level. For force-derived logarithmic decrements (FDLDs), slosh-mass displacement (the displacement of the slosh mass along the forced direction) is a good metric for comparing multiple tests at different wave heights across fill levels because the calculation of it involves dividing by the

slosh mass. For wave-height derived logarithmic decrements (WHDLDs), plotting against wave height makes the most sense, though the wave heights are heavily affected by surface waves and splashing.

The following figure is a plot of FDLD versus slosh mass displacement for the four tests with water at 70% volume fraction. FDLDs were computed using the multiple exponential fits methods (see Section 4.4.1). The shape of the curve is similar for all volume fractions: the FDLD increases towards smaller slosh mass displacements, peaks, and then drops off. Some fill levels had a tendency to start off-axis sloshing, which was truncated from the data, so those cases did not peak. The higher wave amplitude tests in Figure 23 show an increase in FDLD at high slosh mass displacements; this is from wave break/highly nonlinear sloshing, and was seen in a few of the other tests even though the test normal damping procedures were designed to exclude this region.

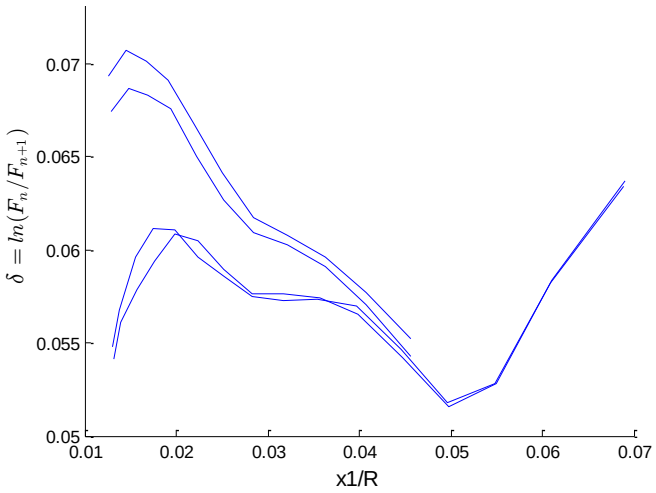

Figure 23. FDLD vs. x1/R for 70% Volume Fraction of Water

While not depicted here, approximately 40 separate damping experiments with water and LN_2 were conducted in the nonlinear region. For LN_2, these tests generally had higher average FDLDs than normal damping tests, and the FDLDs tended to increase with increasing slosh mass displacement. For water, these tests generally showed similar FDLDs to normal damping tests (see two right most curves in Figure 25), and some tests exhibited the characteristic increase in FDLD at high slosh mass displacements. However, most of the nonlinear tests had to be truncated a few seconds after excitation due to off-axis sloshing.

The following figure is a plot of WHDLD versus non-dimensional wave height for the same four tests. WHDLDs were computed using the multiple exponential fits methods (see Section 4.4.1). Note how the curve shape is similar to the FDLD plot. This suggests a real phenomenon and not sensor error. Also, while the higher

amplitude FDLDs and WHDLDs are similar, the lower amplitude WHDLDs are 2-3 times higher than the FDLDs. This behavior was typical across fill levels.

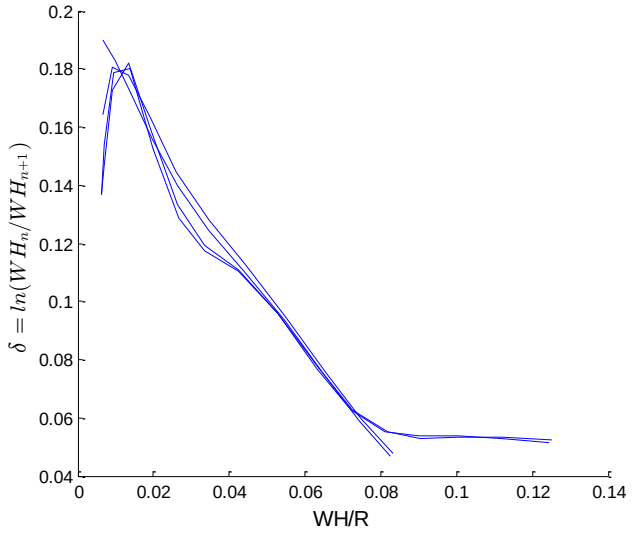

Figure 24. WHDLD vs. WH/R for 70% Volume Fraction of Water

The increasing logarithmic decrement with decreasing wave amplitude trend was not seen in the LN_2 tests, nor in any of the CFD. In fact, after smoothing out the numerical noise and ignoring high amplitude nonlinear sloshing, the equivalent LN_2 plots are essentially straight lines. Because the surface tension is eight times lower for LN_2 than water, and because surface tension was not modeled in the CFD, a surface tension effect might be the cause of the high damping at low wave amplitudes for water. As the inertial forces damp out, they become around the same order of magnitude as the surface tension forces, i.e. We≈1, which lends support to the theory. The damping chapter in [6] has some information on low amplitude wave dynamics; the sources cited there give two possible causes: 1. capillary-

hysteresis (a surface tension effect that creates dissipative force near the contact line) and 2. surface film contamination (a viscosity effect caused by a thin film on the fluid interface). In an attempt to test the surface tension hypothesis, a CFD case with water at 60% fill level with a special refined mesh (see Figure 20) was run with and without surface tension and compared to the experiments. The follow figure is a plot of these results.

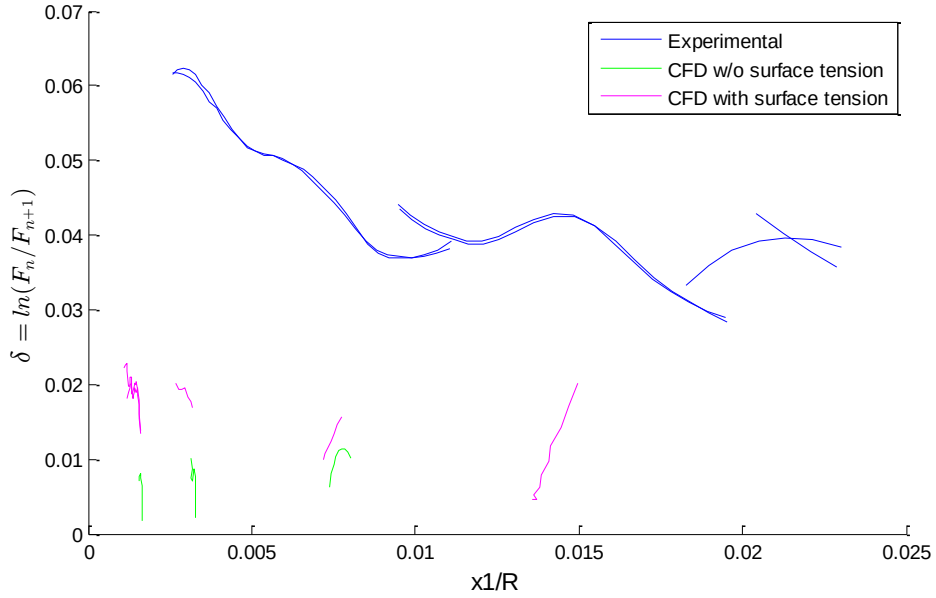

Figure 25. FDLD vs. x1/R for 60% Volume Fraction of Water

The reason the higher amplitude (higher slosh mass displacement) experimental curves do not continue to as low of a x1/R as the lower amplitude experimental curves is because those cases tended to start off-axis sloshing, and so that part of the data was cut out. The no surface tension CFD FDLDs are approximately 4-6 times lower than the experimental results. The CFD cases with surface tension had

more damping than the corresponding without surface tension cases, implying that surface tension is having a significant effect. However, the results are approximately 3 times lower than the experimental FDLDs, and surface tension seemed to have less of an affect for larger slosh mass displacements. A time step of 0.0005 s was used for a repeat of one of the surface tension cases, but this had a negligible effect. A few conclusions can be drawn: 1. Surface tension is important for accurately predicting low amplitude water slosh damping, 2. The mesh may need to be refined, 3. Another physical phenomenon not being modeled might be causing higher experimental damping, e.g. surface film contamination.

An explanation for why the dependence of damping on low wave amplitudes is not described in the literature could be because most past spherical slosh testing was done in larger tanks, e.g. a 32 in diameter tank [27]. The We, Bo, and Re numbers are all larger in larger tanks, implying that gravity and inertial forces heavily dominate surface tension and viscous forces. Typically, spacecraft and rocket designers are not concerned with low amplitude sloshing, and they are usually interested in achieving a minimal level of damping, i.e. any extra damping is usually advantageous. This phenomenon was not observed with LN_2, so it may not be of concern to cryogenic liquids. However, this also implies that water is a poor analog for LN_2 for unrestricted damping predictions because using (viscosity corrected) results from water tests might result in an *over*estimated damping factor.

And while low amplitude sloshing may not be of much concern to the aerospace community, the increase in damping due to nonlinearity at high slosh mass displacements mentioned for Figure 23 could be an important future research topic. While some experiments were performed to examine this regime, more need to be done. No CFD simulations of the nonlinear experiments were completed.

Figure 26 is a comparison between the damping correlations, Eqs. 3.5-3.10, and data from [24] and [27]. The working fluid in all cases was water, and the correlations were calculated for a 32 in diameter tank. For reference, the X_0/D for damping tests in this project ranged from 0.0017 to 0.0067, which is around the same range as the upper three experimental curves. Figure 26 provides a sense of the order of magnitude, variance, and error relative to the correlations to be expected from the logarithmic decrements from this project.

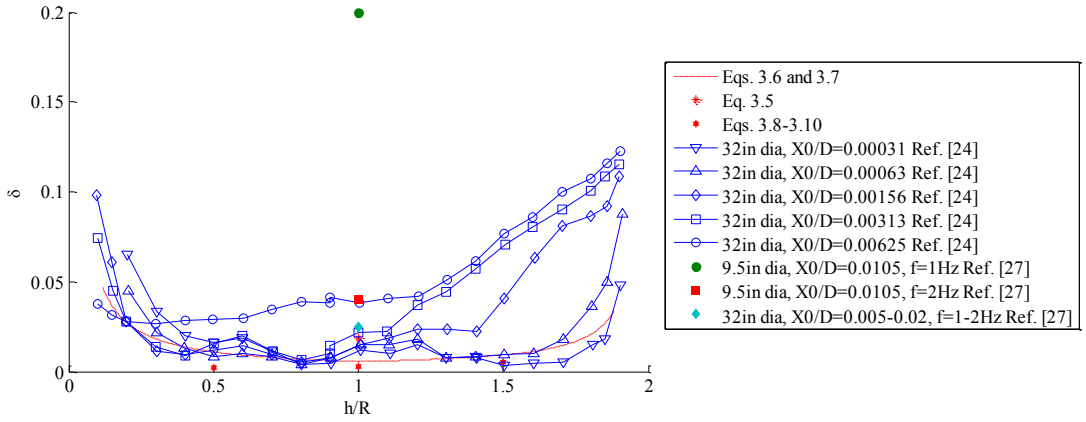

Figure 26. Damping Correlations vs. Past Experimental Data

Clearly there is a dependence on excitation amplitude. Because of the way those tests were conducted, different excitation amplitudes and numbers of cycles will result in different wave amplitudes, so I argue that the real, direct dependence of damping is on wave amplitude or slosh mass displacement, and not on excitation amplitude or excitation frequency. Unfortunately, the wave amplitudes from those tests were not published. The correlations underpredict logarithmic decrement for the majority of Figure 26. The following discussion will regard only the largest three excitation amplitude data series. All of the correlations underpredict the results for fill fractions greater than or equal to 1, with an error of 400% or more for some points. For fill fractions less than one, the correlations usually underpredict, but sometimes over-predict, the logarithmic decrement. The curve defined by Eqs. 3.6 and 3.7 does not adequately capture the shape of the data curves for any of the results. The shape disagreement is most extreme for large amplitudes, where the logarithmic decrement is generally lower for low fill fractions and higher for high fill fractions, though the upward trends for the lowest and highest fill fractions are present in both the Eqs. 3.6 and 3.7 correlation and the data. Also note the local maxima around fill fractions of 0.6 and 1.2 for some of the data series; it is unclear what caused these. The Eqs. 3.8-3.10 correlation points underpredict the results for all but one point, and the Eq. 3.5 correlation performance is mixed. Because of the large difference between the correlation and the data for the three largest excitation

amplitude cases, it is highly likely that the slosh was nonlinear for fill fractions greater than 1.

The following two figures are constructed by averaging all of the (lateral) damping data for each test and CFD case and plotting these points versus fill fraction. Note that CMDLDs are derived from the center of mass displacement, which can only be obtained from CFD. “NB” and “NL” stand for no-boiling and nonlinear respectively.

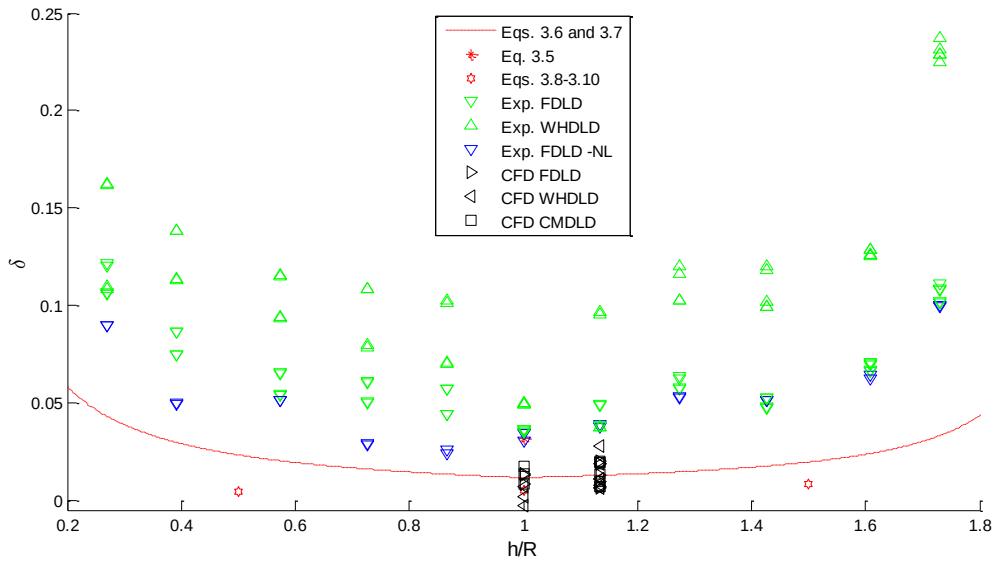

Figure 27. Logarithmic Decrement vs. Fill Fraction - Water

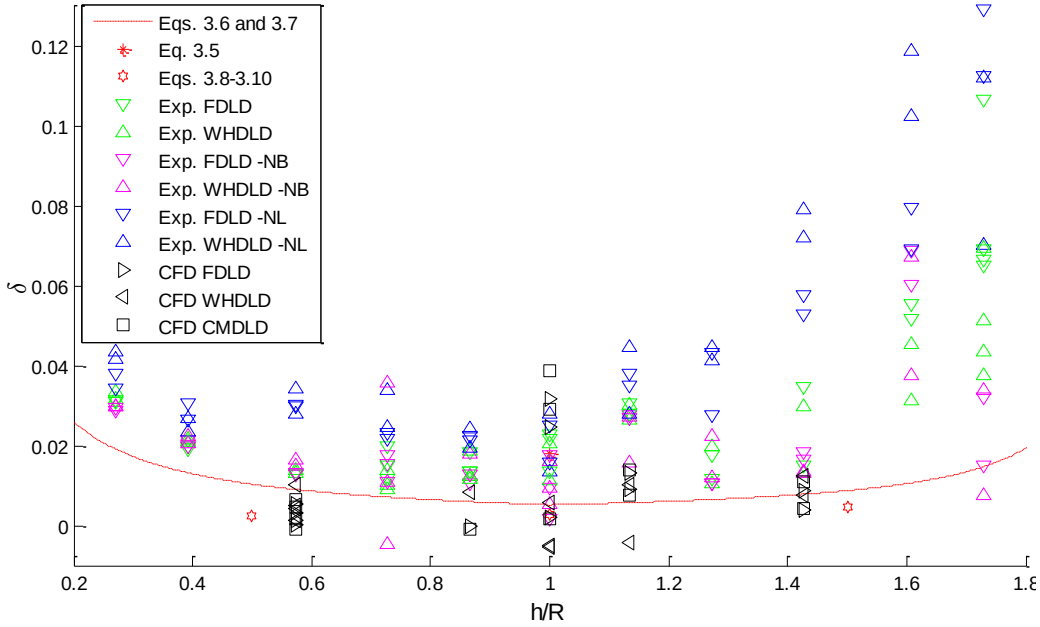

Figure 28. Logarithmic Decrement vs. Fill Fraction – LN_2

The pairing and clustering of experimental points in Figure 27 are due to repeated tests and different wave amplitudes. Most of the experimental FDLDs are all higher than the correlations by about a factor of 2. The general trend for both FDLDs and WHDLDs is similar to the correlations though: increasing towards low fill fraction and high fill fractions [5]. Since the nonlinear damping tests exhibited splashing and higher amplitude motion, it was expected that the damping would be higher than the normal damping tests. However, this was not the case for water. For lower volume fractions, the nonlinear FDLDs were generally lower than the normal FDLDs. This is because the nonlinear FDLDs were computed with the majority of the low amplitude (highest damping) slosh truncated due to off-axis sloshing. The nonlinear FDLDs for the higher volume fractions tended to be within 10% of the

normal FDLDs. The error of the CFD results in Figure 27 relative to the experimental results and correlations is generally within 100% and 20% respectively. The better agreement with the correlations supports the earlier conclusion that a physical phenomenon present during the water testing is not being modeled in the CFD (see previous nondimensional parameter discussion). Note that two of the CFD WHDLDs at 50% were negative; this is due to the WHDLD's sensitivity to surface waves. For a surface wave to affect the fluid sensor reading, it must be of high enough amplitude to flow around and between the plates. In the CFD, there is no plate, so any surface waves or ripples are registered by the fluid sensor simulator field function. The WHDLDs are consistently higher than the FDLDs in Figure 27, but they are not in Figure 28, suggesting that the extra apparent wave height damping is a function of viscosity. This could be a result of fluid sensor error where increased wave height damping is seen between the fluid sensor plates due to viscous drag, while the actual wave amplitude is not damped as much. The compensation efforts discussed in Section 4.3.5.4 were supposed to correct for that kind of error, but they may not have worked well enough.

Figure 28 shows similar levels of agreement between the experiments, CFD, and correlations, with errors generally around 50-100%, though some logarithmic decrements, particularly from nonlinear tests, were up to 7 times higher than the correlations. The nonlinear damping tests exhibited higher average damping than

normal tests, which was the expected trend (and the opposite trend compared to water). This is because the mechanism present for the water tests that causes the logarithmic decrements to increase as the slosh mass displacement (or wave amplitude) decreases is not present in LN_2 tests. The upward trend towards lower and higher fill fractions is present in Figure 28, as it was in Figure 27. No significant difference was seen between the normal and no boiling experiments, likely because the natural convection currents, which had a visibly greater effect on the flow than the boiling, did not stop during the no boiling testing. The CFD damping factors for 20% and 40% volume fractions were almost 0. The 20% CFD cases were redone with a with a time step of 0.0005 s and a mesh refined in the lower half the tank; this resulted in logarithmic decrements 2-3 times higher than first set, but still close to 0. Two CFD WHDLDs, one at 50% and one at 60%, were negative for the same reasons mentioned above. Two of the 50% volume fraction CFD cases had FDLDs about two times higher than their corresponding experiments. The differences between the CFD and experiments cannot be accounted for, though the lack of mesh and time step independence are the most likely causes. The natural convection boundary layer present in the experiments may have increased the effective damping; since the CFD was isothermal, no natural convection was present in the numerical results. While the the low CFD results for 20% and 40% volume fractions support this line of reasoning, the CFD results at 50% do not.

The small bump around fill fraction of 1.2 or 1.3 that was visible in Figure 26 is visible in the experimental data of Figure 27 and Figure 28. It is unclear what physical phenomenon is causing this. Also visible in both figures is the large difference (factor of ~3-7) between experimental and correlation damping values at 95%, as well as at 90% in Figure 28. The wall curvature at 90 and 95% promotes wave rolling and nonlinear sloshing, and nonlinear sloshing generally results in higher damping. The logarithmic decrements for LN_2 are 2-3 times lower than for water (on average), which makes physical sense because lower viscosity fluids experience less viscous damping.

It is worth noting that these experimental results differ from last year [25] by up to 500%. The differences are attributable to two sources: 1. the way the tank was excited last year for damping cases was different than this year, and 2. the experimental setup last year was different and less accurate.

The (usually) under-predictive nature of the Eqs. 3.6 and 3.7 correlation is useful because having more damping is usually better than less damping in tank design, but this correlation is limited to purely 1-axis lateral slosh. Even the idealized case of 1-axis lateral slosh in spherical tanks is a fundamentally non-linear process for not-unreasonably large amplitudes. Finding a useful empirical damping correlation that accounts for the nonlinear effects of wave amplitude or slosh mass displacement might be possible, but will require substantially more experimental

data to develop. Another conclusion is that FDLDs should be used in place of WHDLDs whenever possible; fortunately, forces are easier to obtain experimentally and in CFD than wall heights.

The primary conclusion that can be drawn from the damping portion of this project is that, while it is possible to perform CFD simulations of this fidelity that agree with experimental damping factors within 10% (also see [12]), the variance in experimental data and the CFD means that firm validation is impossible. More experimental damping data needs to be collected in order to reduce uncertainty. It is likely that higher fidelity CFD is necessary in order to accurately *and consistently* predict damping in spherical tanks. If refined meshes and smaller time steps do not yield results that agree better with the experiments for LN_2, non-isothermal modeling needs to be explored. Another conclusion is that water is a poor analog for LN_2 for determining damping factors, at least for tanks of this size. It may be that the phenomenon of increased damping for low wave amplitudes becomes insignificant in larger tanks. The exact mechanism causing this phenomenon is unknown, and it does not appear to be modeled in the CFD.

It was reasoned that the effect of the fluid sensor on the damping results should be small because its surface area is small compared to the tank's surface area. To test this theory, 6 water experiments were repeated without the fluid sensor.

Comparison to experiments with the fluid sensor showed that the sensor has no significant effect on the damping.

6.2 Damping with a Baffle

The experimental data, numerical data, and theory for damping with a ring baffle will be presented in this section. The baffle considered is an annular ring located at the 50% level with a w/R = 0.125. Approximately 50 experimental baffle damping tests were conducted. Seven CFD baffle damping cases were completed, three for water and four for LN_2.

The following two plots depict experimental and CFD first mode frequencies computed by FFT of force decay waveforms for water and LN_2. The unrestricted theory for the first mode is also included in the plots for reference. Figure 29 includes data from [26].

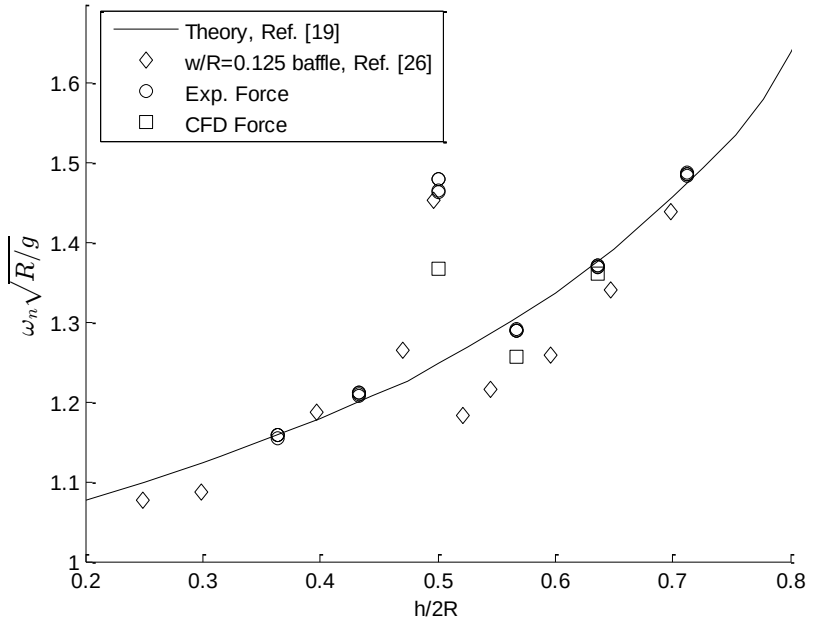

Figure 29. 1st Mode Frequency Parameter vs. Fill Fraction for Water with a Baffle

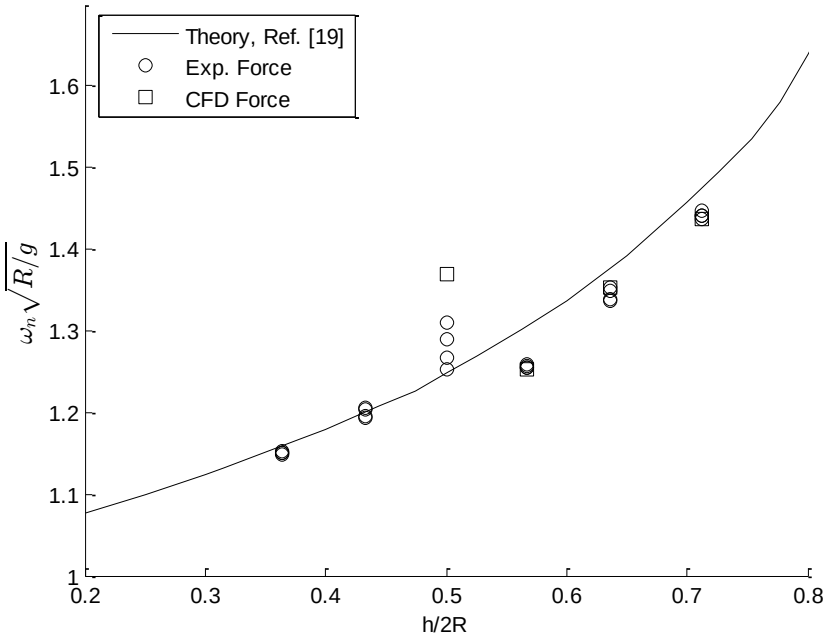

Figure 30. 1st Mode Frequency Parameter vs. Fill Fraction for LN_2 with a Baffle

The spike in frequency at the baffle location is due to the baffle effectively causing a reduction in diameter, and smaller diameter tanks have higher resonant

frequencies. The subsequent drop in frequency at fill levels immediately above the baffle is probably due to the baffle decreasing the effective liquid depth. [26] The current experimental and CFD data seem to be within 10% error relative to an imagined faired curve for the past data in Figure 29. The experimental values from this project volume fractions above the baffle tended to be 5-10% higher than past data, though an experiment would need to be run at an h/2R of around 0.55 to confirm this trend. No prior data exists for LN_2 in a tank with a ring baffle, so all of the data in Figure 30 is from this project. Except at 50%, error between the CFD and experimental data within 2%. The spread at 50% volume fraction can be attributed to the rapid change in frequency at liquid depths just above the baffle level. Due to the error in gauging LN_2 volume with the ruler, it is possible that these tests were done with too much LN_2.

The following plot compares past baffle damping data from a 32 in diameter tank with water [26] to the baffle theory presented in Section 3.4. The purpose of this plot is to give a sense of the expected error of experimental baffle damping data with respect to the theory. Note that wave amplitude, which is necessary for the theory's formula, was not published. A best guess of the average wave amplitude was determined by trial and error and found to be 0.042 m.

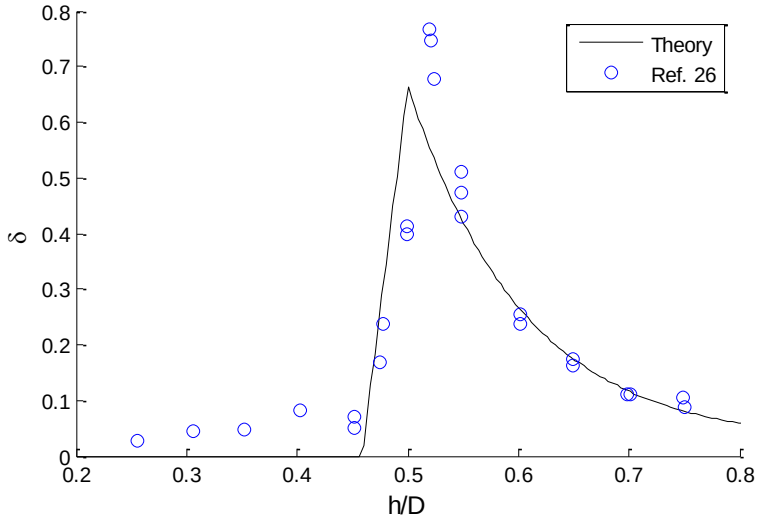

Figure 31. Logarithmic Decrement vs. Fill Fraction – 32 inch Baffled Tank with Water

In Figure 31, note how the experimental data peaks before the baffle location. This is typical of this theory [4], i.e. this theory tends to underpredict the damping in the region just above the baffle. Since having more damping than predicted is generally ok for tank slosh, this theory is commonly used. However, it does tend to over-predict damping when the static fluid level is right at the baffle location.

A discrepancy between some past no baffle damping data was discovered while examining the plot that yielded the data in Figure 31. In the original plot, a set of no baffle damping data is presented for comparison. However, it is an order of magnitude lower than the damping data presented in the original figure reproduced in Figure 26. The same tank, X_0/D, and fluid were used in both, and the test procedures' descriptions ae essentially identical. Except for a reporting mistake, the

only difference could be a difference in number of cycles resulting in a difference in wave amplitudes.

The following plots compares experimental and numerical baffle damping results to the theory. WHDLDs were not included in these plots for two reasons, clutter and having more confidence in the FDLDs. Also, 50% water cases did not register high enough wave amplitudes to generate WHDLDs; this was not a fluid sensor error because the videos clearly show almost no wave amplitude growth for both water and LN_2 at 50%. For the 30 and 40% volume fraction tests, the portion of the data after the point when the fluid surface stopped making contact with the baffle was cut out.

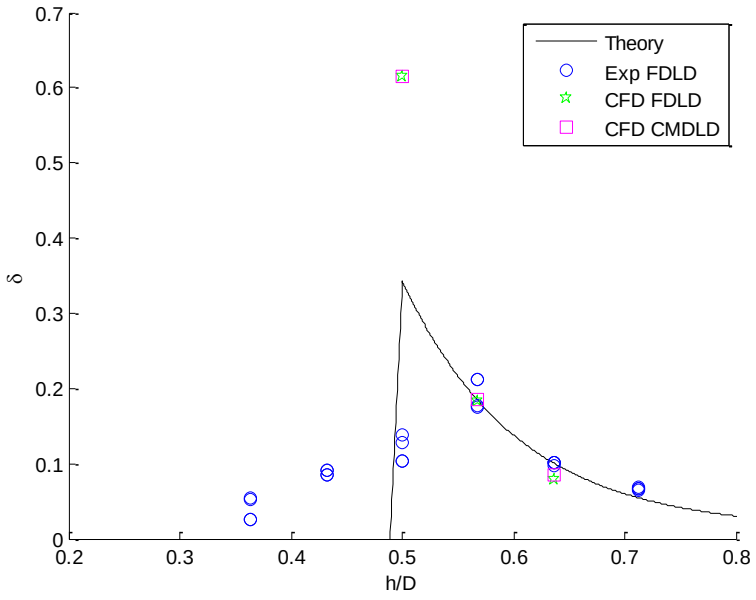

Figure 32. Logarithmic Decrement vs. Fill Fraction –Baffle, Water

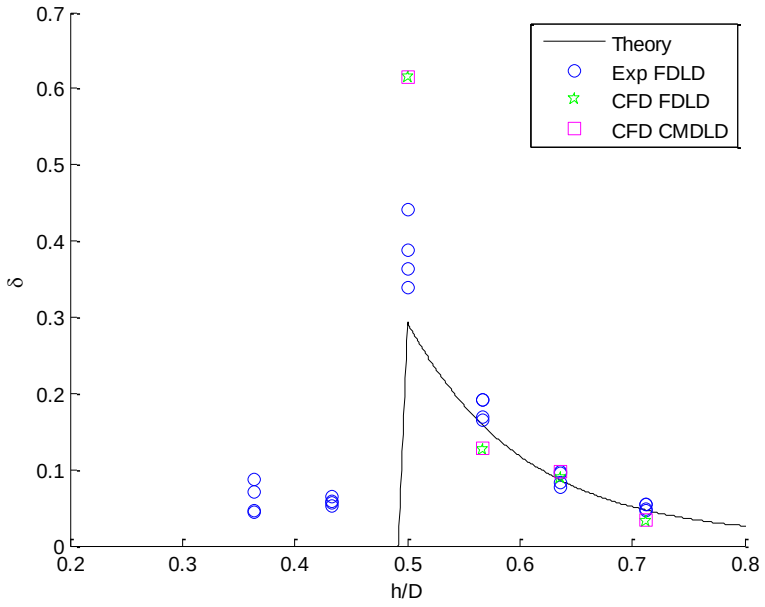

Figure 33. Logarithmic Decrement vs. Fill Fraction –Baffle, LN_2

Figure 32 and Figure 33 show errors less than 30% between CFD and experiments for 60, 70, and 80% volume fractions. However, the CFD over-predicted the damping at 50% for both fluids, by about 400% for water and 50% for LN_2. Examining the videos of the experiments and the CFD shed some light on the matter. The CFD cases at 50% achieved a higher wave height than the experiments, particularly for water. Because the fluid was so effectively damped for 50% water experiments, the damping factor is actually lower than would be expected. Something similar happened in the LN_2 experiments, though to a lesser extent. It is unclear why the water experiments did not achieve higher wave heights. It must be noted that the theory lines shown in Figure 32 and Figure 33 were computed using a wave amplitude about 50% of the measured average wall height because using

the measured value resulted in theory lines far above the experimental results. It is unclear why this is the case. The best guess is that splashing, ripples, or vortices caused by the baffle, coupled with the hole in the baffle around the fluid sensor, skewed the averaging wall height scheme, which works by averaging maxima. Comparisons to Figure 27 and Figure 28 indicate that the baffle was more effective for increasing damping with LN_2 than water, though (disregarding the WHDLDs Figure 27) the average damping was increased for water as well. This is likely because baffle damping is primarily dependent on pressure drag, while non-baffled damping is dependent primarily on viscous damping.

It seems that the key to using the theory in design work is getting an accurate average measurement or estimate of wave amplitude. However, the baffle influences the wave amplitude, so it becomes a cyclic design problem. Fortunately, CFD of this fidelity seems to be adequate for predicting ring baffle damping for water and LN_2 at most volume fractions, though accurately predicting damping for fluid levels right around the baffle will probably require a finer mesh and smaller time steps. Also, turbulence modeling does not seem to be necessary since the laminar CFD over-predicted the damping at least 50%; this is good because even a basic RANS turbulence model can double the computation time of a slosh simulation.

6.3 Forced Excitation

The experimental data, numerical data, and analytical solution for forced sinusoidal excitation will be presented in this section. Approximately 270 experimental forced excitation tests were conducted for two volume fractions for water, 20 and 50%, and four volume fractions for LN_2, 20, 50, 60, and 80%. 14 CFD forced excitation cases were completed, three for water and eleven for LN_2.

The following five plots are time domain comparisons of experimental, numerical, and analytical results of force and wave height for LN_2. The experimental and analytical results are truncated to the length of the CFD solution. The CFD wave height from the case in Figure 38 is not included because the fluid sensor emulator function was on the opposite side of the tank (see discussion in Section 5.1.5). This was amended for the cases presented in Figures 35 and 37, which were re-run with the emulator on the correct side of the tank and with a time step of 0.0005 s instead of 0.001 s.

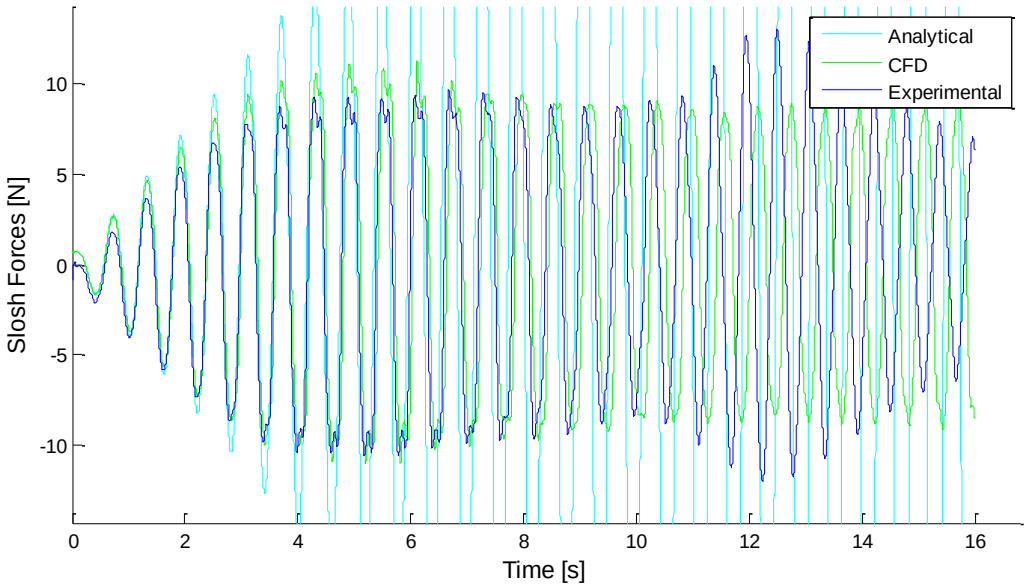

Figure 34. Slosh Forces vs. Time: LN_2, 60%, X_0=1.866 mm, f=1.685 Hz

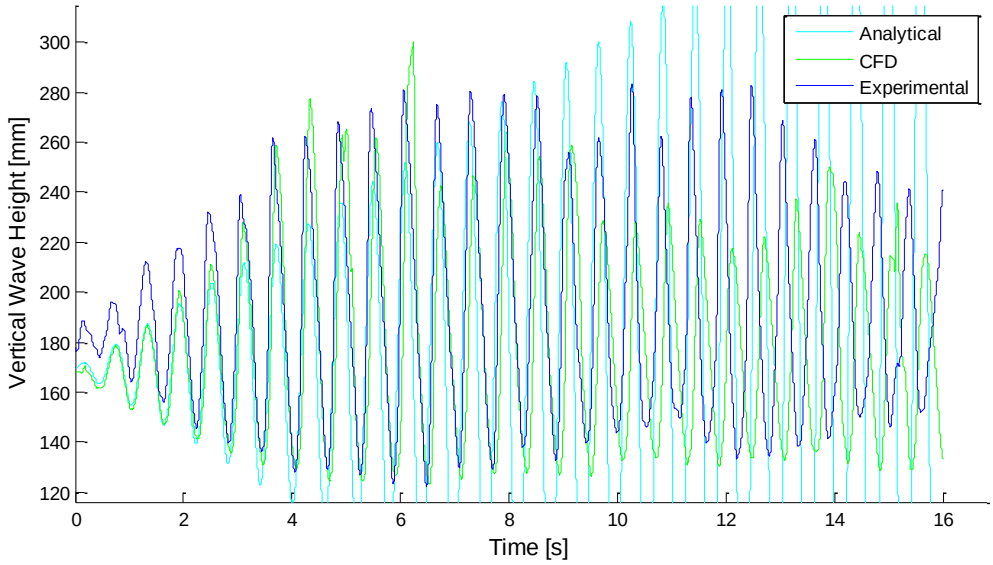

Figure 35. Wave Height vs. Time: LN_2, 60%, X_0=1.866 mm, f=1.685 Hz

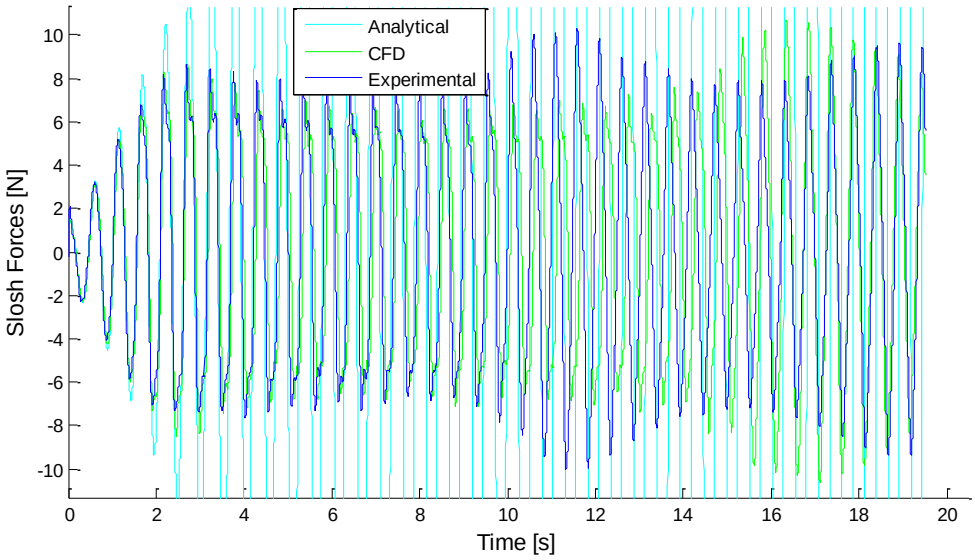

Figure 36. Slosh Forces vs. Time: LN_2, 80%, X_0=1.866 mm, f=1.903 Hz

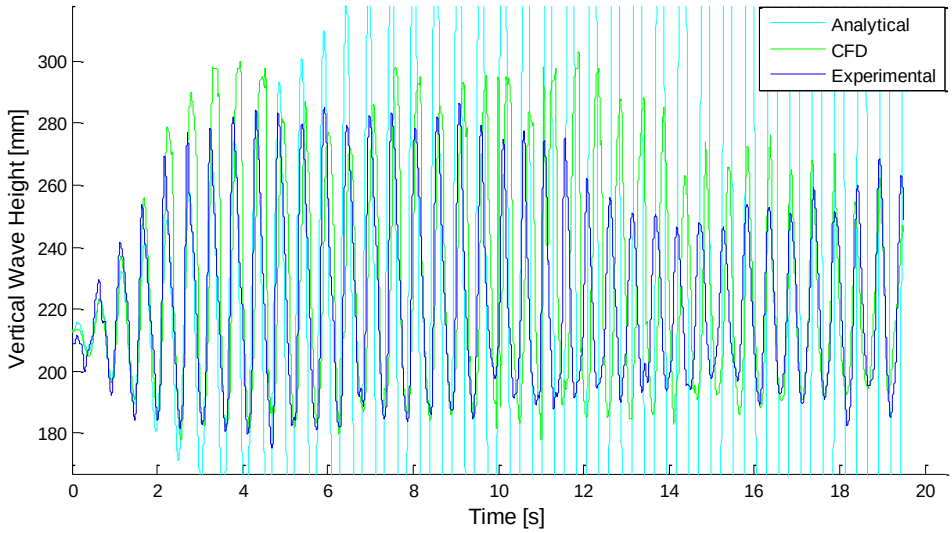

Figure 37. Wave Height vs. Time: LN_2, 80%, X_0=1.866 mm, f=1.903 Hz

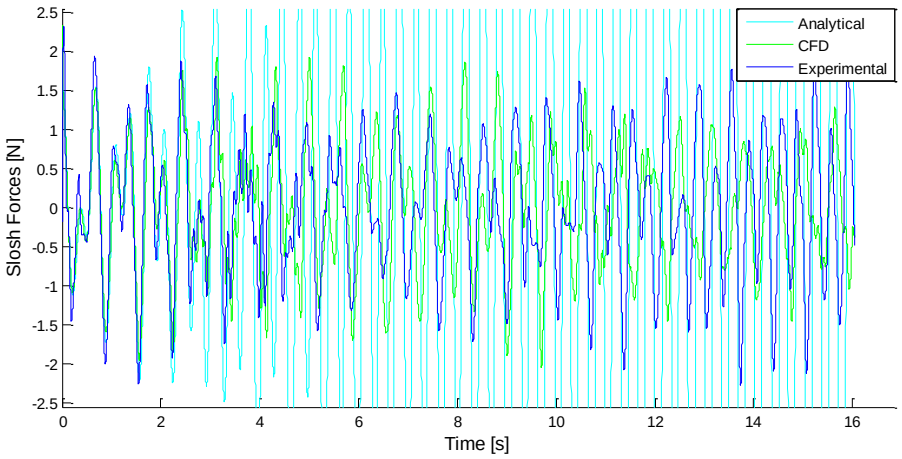

Figure 38. Slosh Forces vs. Time: LN_2, 50%, X_0=2 mm, f=2.96 Hz

The analytical solutions grow to infinity because these cases were forced a resonant frequency and the analytical derivation assumed an inviscid fluid. The analytical solutions are plotted in a lighter color so that they do not obscure the experimental and CFD results. All errors between experiment and CFD of the force plots' peaks for the first few seconds are within 10%, and generally stay within 20% for the majority of the waveforms. Even if the force peaks do not line up in time, the amplitudes of surrounding peaks are usually within 20%. The exception is during the rotational "pulses", such as the ones centered around 12 s in Figures 34 and 36. The CFD did not predict the onset of rotation at the correct times, though a rotational pulse is present starting around 15 s in Figure 36. Examining the experiment and CFD videos of that case show many qualitative similarities. The discussion in Section 4.6.4 elaborates on rotary sloshing. The CFD wave height peaks in Figures 35 and 37 tended to be within 20% of the experimental results, but

as mentioned for the force plots, the CFD does not predict the onset of rotation at the correct times. While rotation causes a phase difference between the CFD and experimental results, there is also a smaller lag present in the CFD that seems to grow steadily; this is likely time discretization error and/or too large of a time step. Decreasing the time step from 0.0005 s to 0.001 s seemed to decrease this lag. Decreasing the time step also made the rotational pulse in Figure 36 occur approximately 3 s earlier. It appears that the fluid sensor had an initial positive offset in Figure 35. Figure 38 is of excitation at the 2nd resonant frequency of 50% volume fraction. Examination of both experiment and CFD videos reveals a stable 2nd mode during the first few seconds before wave break and collapse.

While rotary slosh is shown in some of the above figures, those portions of the experiment and simulation were cut out for the analyses discussed below.

The following four figures are plots of the slosh force parameter, $F_{max}/\rho g D^2 X_0$, versus the frequency parameter, $\omega\sqrt{R/g}$, at 20, 50, 60, and 80% volume fraction. Each point is generated by finding the maximum lateral slosh force of each test or CFD case. Because the force parameter is nondimensionalized by the fluid density and the excitation amplitude, tests of different fluids and excitation amplitudes can be compared. The theory line is generated from the method described in Section

3.2. These figures give a sense of the frequency response of the tank at each fill level.

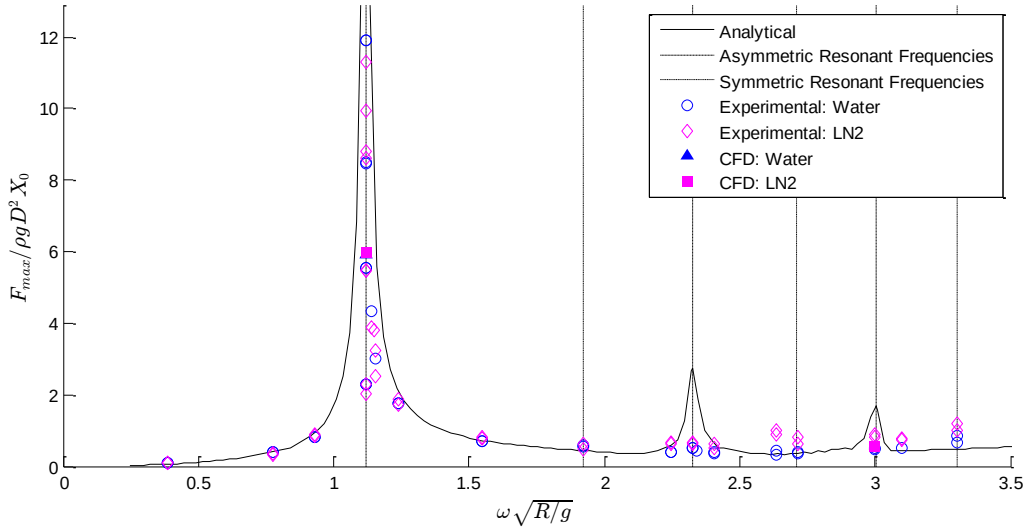

Figure 39. Slosh Force Parameter vs. Frequency Parameter: 20%

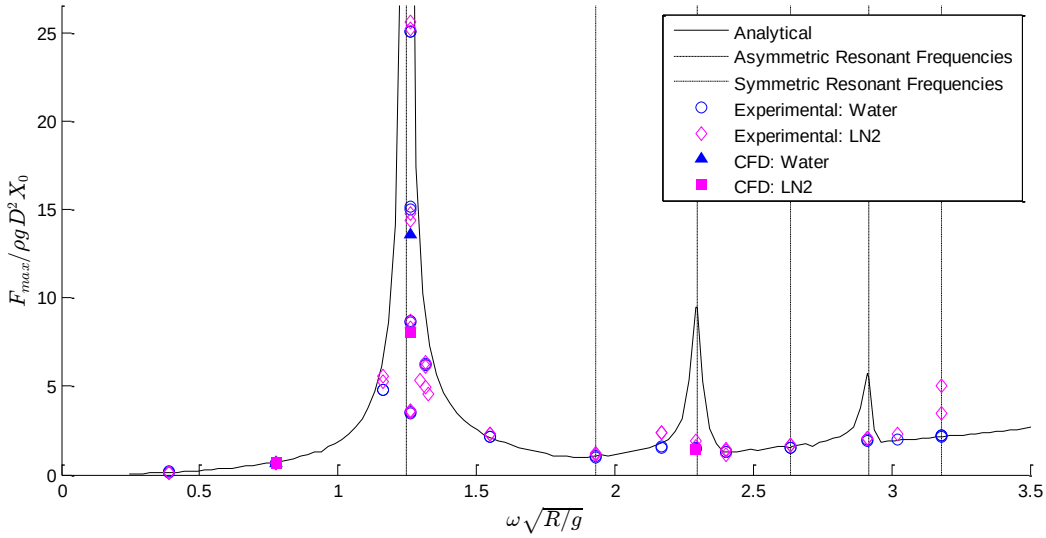

Figure 40. Slosh Force Parameter vs. Frequency Parameter: 50%

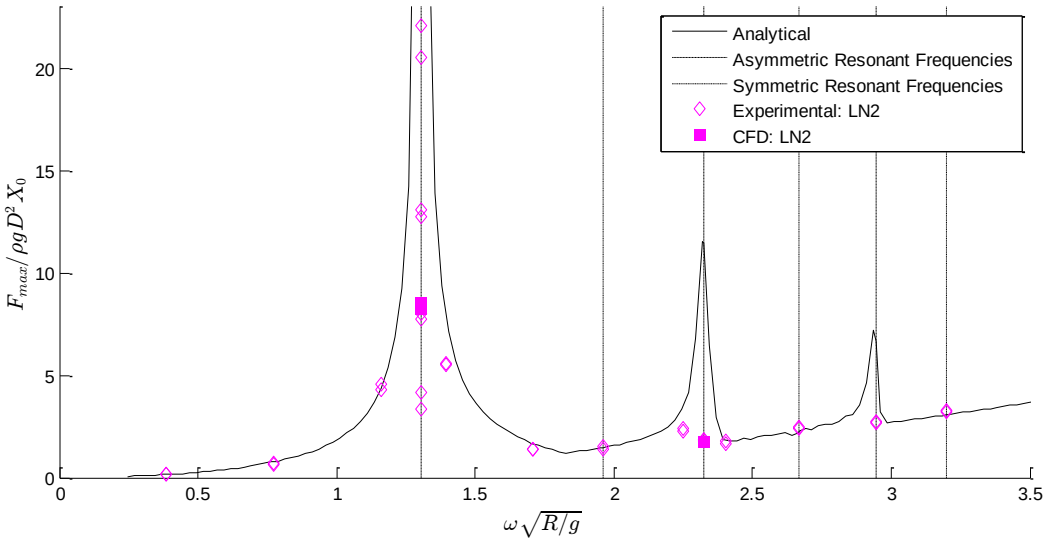

Figure 41. Slosh Force Parameter vs. Frequency Parameter: 60%

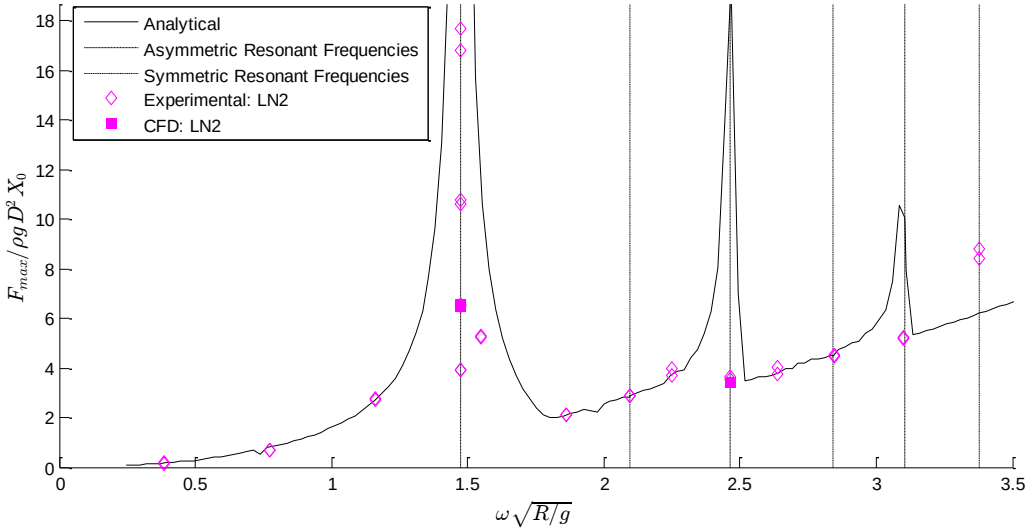

Figure 42. Slosh Force Parameter vs. Frequency Parameter: 80%

Error between theory and experiments for all figures and most frequencies is usually within 5%, with the notable exception of the resonant frequencies. This is because the theory does not account for viscous damping, which prevents the slosh

at resonance from growing to infinity. The spread of points, usually in clusters, on the 1st mode resonant frequency line are from repeated tests at four different excitation amplitudes, 0.466 mm, 0.934 mm, 1.866 mm, and 6 mm. The largest excitation cases have the lowest force parameters and the smallest excitation cases have the highest because the maximum force does not grow linearly with excitation amplitude. No 2nd or 3rd modes were strongly, directly excited in the experiments or CFD (see Figure 40), though examination of the videos shows that they were present (when forced at their respective resonant frequencies) for a few seconds before the onset of rotation and/or chaotic sloshing. No symmetric modes were excited, which is not surprising because vertical excitation is (usually) required to excite those modes. Some of the higher frequency LN_2 tests showed larger errors relative to the theory. For example, at the highest tested frequency for LN_2 in Figure 40 and Figure 42, the error relative to the theory is about 50%. The videos depict a "weird", high amplitude mode developing during those tests that is likely a combination of multiple modes. In Figure 39, the two CFD cases (one water and one LN_2, both X_0=1.866 mm) are overlapping near the 1st mode 1.866 mm excitation tests' points. There are five CFD points in Figure 40: one water and LN_2 at 1 Hz, one X_0=0.934 mm water case near the 1st mode 0.934 mm excitation tests' points, one X_0=1.866 mm LN_2 case near the 1st mode 1.866 mm excitation tests' points, and one LN_2 at 2.96 Hz (2nd mode). There are three CFD points in Figure 41 and Figure 42, two at the 1st mode resonant frequency and X_0=1.866 mm that were

run with different time steps. All CFD points' errors relative to the experiments are within 50%, and most are within 10%. These results are supported by last year's results, which were done in a similar manner with the previous iteration of the current test setup. [25]

The following figure is a plot of the non-dimensional 1st mode slosh force parameter, $F_s/\rho g D^3$, versus fill fraction and the non-dimensional excitation parameter, X_0/D. The difference between the slosh force parameter in Figures 39-42 is that this one is calculated only from the first mode resonant frequency tests and the X_0 in the denominator of the previous force parameter's definition is replaced by another D. The past data included in the plot is from a 32 in diameter tank with water. [24]. All tests of the same fluid were made the same color, each X_0/D was assigned a symbol, and CFD symbols were filled in.

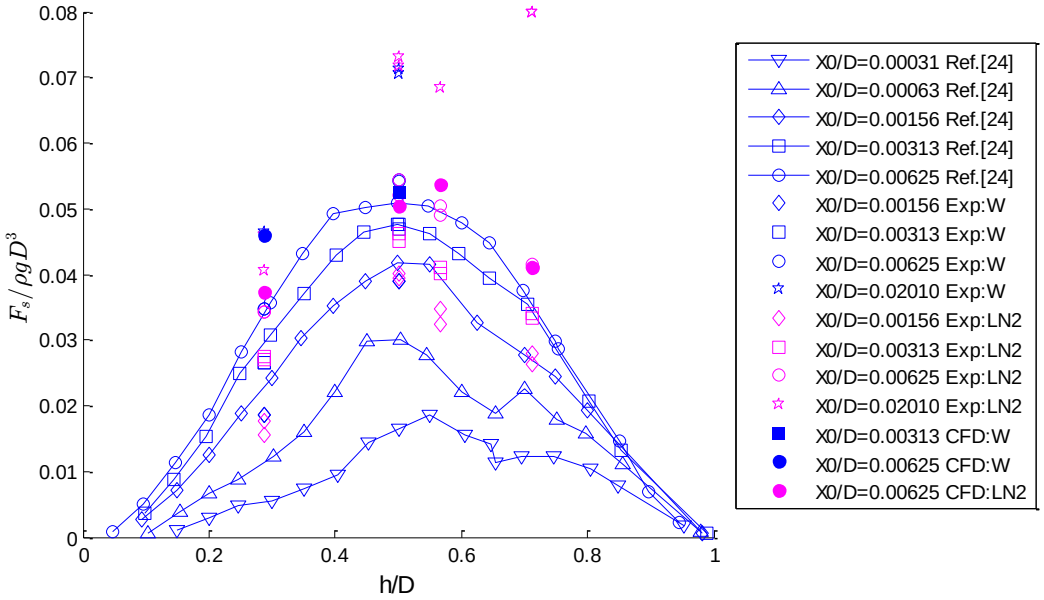

Figure 43. 1st Mode Slosh Force Parameter vs. Fill Fraction

Maximum slosh force is clearly dependent on both fill fraction and excitation amplitude, both of which make physical sense. The past and current experimental results are generally within 10%, though a few cases saw closer to 20% error. All of the $X_0/D=0.02010$ points are higher than the other points, which makes physical sense because higher excitation should result in higher forces. It is hard to tell from only four fill fractions, but it seems that the shape for the $X_0/D=0.02010$ curve would be correct except for the 80% point being too high. Interestingly, the $X_0/D=0.00625$ 80% experiment and CFD were also above the past data, so a difference in the way the experiments were performed likely accounts for the difference in shape. The experiments that generated the past data were stopped before significant splashing occurred, while the forced excitation tests in this

project were continuously excited regardless of splashing. Since higher excitation amplitude tends to cause higher amounts of splashing, the past data experiments were likely stopped before the maximum force could be achieved. The 20%, $X_0/D=0.00625$ water CFD case over-predicts its respective experiment by about 30%; it is not clear why this was the case.

More cases need to be run, but these initial results show that the CFD is sometimes capable of accurately predicting slosh forces and wave height for unrestricted continuous lateral excitation. Even if the slosh forces and wave heights versus time were not identical, the dominant amplitudes, characteristics, and fluid motions were present in both CFD and experiments, implying that no major mistakes were made in the CFD methodology. These results also show that the analytical solution computed from the first three asymmetric modes is adequate for predicting maximum slosh forces for excitation frequencies not near resonant frequencies.

Chapter 7 Conclusions and Future Work

The experimental objective of this project was met. Spherical tank slosh data for water and LN_2 relevant to CFD validation was successfully collected. The numerical and validation objectives were partially met. Approximately 40 CFD simulations of water and LN_2 in the spherical tank were completed. Judging from level of agreement between the experiments, CFD, and various theories, there is some confidence in the CFD models used in this project to accurately predict lateral fluid slosh, particularly for slosh forces. However, it is also clear that more, and higher fidelity, CFD cases need to be run before validation can be claimed.

Various avenues to improving the CFD methodology need to be explored. The mesh and time step dependence study needs to be continued, and the mesh and/or time step should be refined based on the results. Inclusion of the non-constant density, thermal, and evaporation models for LN_2 slosh simulations would probably improve accuracy, though at the expensive of more computational time.

While the majority of the future work is related to the CFD, some extended experiment objectives exist. More rigorous uncertainty analyses and more repeated experiments would improve confidence in the experimental data. While the current damping correlations may be sufficient for determining a lower bound on damping

factor, a more advanced damping correlation should be developed that takes into account wave amplitude or slosh mass displacement. The fluid sensor needs further development to increase its accuracy and commercial viability.

Near-term plans include performing 3-DOF couple slosh-motion testing on the FIT Orion Laboratory's flat floor using the current "floating frame" test setup decoupled from its actuator. Various "push types" and volume fractions for both water and LN_2 will be tested. Frame position and orientation will be tracked with an infrared optical tracking system. Images of the fluid free surface and fluid sensor data will also be collected. The position data during the "push", along with moments of inertia from a computer aided design (CAD) model, will be used to derive 3-DOF forces and moments about the center of the tank for input into STAR-CCM+'s rigid body dynamics solver. The resulting trajectory, wall heights, and images from the CFD will be compared to the same from the experiments.

Rotational slosh modes seem to be particularly important in terms of amplitude and long decay times. More research needs into non-lateral slosh needs to be done, though none is planned by the author at this time.

A final objective is to compile all test and simulation data from this project in the KSC LSP Electronic Slosh Data Catalog (ESCD) by the end of summer 2016 so that it will be available to all NASA and NASA-affiliated slosh researchers.

References

[1] M. D. Berglund, C. E. Bassett, J. M. Kelso, J. Mishic and D. Schrage, "The Boeing Delta IV Launch Vehicle: Pulse-Settling Approach for Second-Stage Hydrogen Propellant Management," *Acta Astronautica,* vol. 61, no. 1-6, pp. 416-424, 2007.

[2] T. E. Strikwerda, J. C. Ray, D. R. Haley and D. J. O'Shaughnessy, "NEAR Shoemaker: Major Anomaly Survival, Delayed Rendezvous and Mission Success," *Guidance and Control,* pp. 597-614, 2001.

[3] E. M. Jones, "The First Lunar Landing".

[4] N. H. Abramson, "The Dynamic Behavior of Liquids in Moving Containers," NASA, Washington, D.C, 1966.

[5] F. T. Dodge, "The New 'Dynamic Behavior Of Liquids in Moving Containers'," SWRI, San Antonio, Texas, 2000.

[6] R. Ibrahim, Liquid Sloshing Dynamics Theory and Applications, New York: Cambridge University Press, 2005.

[7] M. Meyer, D. Chato, D. Plachta, G. Zimmerli, S. Barsi, V. Dresar and J. Moder, "Mastering Cryogenic Propellants," *Journal of Aerospace Engineering,* vol. 26, pp. 343-351, 2013.

[8] J. Agui and J. P. Moder, "Modeling of Non-isolthermal Cryogenic Fluid Sloshing," in *51st AIAA Joint Propulsion Conference,* Orlando, FL, 2015.

[9] NASA KSC, "Cryogenic Slosh Data Final Report (internal document)," 2013.

[10] T. Arndt, M. Dreyer, P. Behruzi and A. van Foreest, "Cryogenic Sloshing Tests in a Pressurized Cylindrical Reservoir," in *45th AIAA Joint Propulsion Conference,* Denver, CO, 2009.

[11] J. Lacapere, B. Vielle and B. Legrand, "Experimental and Numerical Results of Sloshing with Cryogenic Fluids," *Progress in Propulsion Physics 1,* pp. 267-278, 2009.

[12] B. Marsell, S. Gangadharan, Y. Chatman and J. Ristow, "A CFD Approach to Modeling Spacecraft Fuel Slosh," AIAA, 2009. [Online]. Available: http://ntrs.nasa.gov/archive/nasa/casi.ntrs.nasa.gov/20130012592_2013011848.pdf. [Accessed 11 November 2013].

[13] D. Benson and M. Paul, "Method for CFD Simulation of Propellant Slosh in a Spherical Tank," in *47th Joint Propulsion Conference*, San Diego, CA, 2011.

[14] J. J. M. Prins, "Sloshsat FLEVO Facility for Liquid Experiment and Verification in Orbit," in *International Astronautical Congress*, Rio de Janerio, Brazil, 2000.

[15] B. Barshan and D. Baskent, "Comparison of Two Methods of Surface Profile Extraction from Multiple Ultrasonic Range Measurements," *Measurement Science and Technology*, vol. 11, no. 6, pp. 833-844, 2000.

[16] R. Zhou, M. Vergalla, S. Chintalapati, D. Kirk and H. Gutierrez, "Experimental and Numerical Investagtion of Liquid Slosh Behavior Using Ground-Based Platforms," *Journal of Spacecraft and Rockets*, vol. 49, no. 6, 2012.

[17] J. Fraure, M. Vergalla, R. Zhou, S. Chintalapati, H. Gutierrez and D. Kirk, "Experimental Platform for the Study of Liquid Slosh Dynamics using Sounding Rockets," *IREASE*, 2010.

[18] M. Vergalla, R. Zhou, H. Gutierrez and D. Kirk, "Experimental and Numerical Framework for Characterization of Slosh Dynamics," *IREASE*, 2009.

[19] P. McIver, "Sloshing Frequencies for Cylindrical and Spherical Containers Filled to an Arbitrary Depth," *Journal of Fluid Mechanics*, vol. 201, pp. 243-257, 1989.

[20] B. Budiansky, "Sloshing of Liquids in Circular Canals and Spherical Tanks," Lockheed Aircraft Corporation, 1958.

[21] Mathworks, *MATLAB (software)*, 2014.

[22] J. W. Miles, "Ring Damping of Free Surface Oscillations in a Circular Tank," *ASME Journal of Applied Mechanics*, vol. 25, pp. 274-276, 1958.

[23] J. V. Rattayya, "Sloshing of Liquids in Axisymmetric Ellipsoidal Tanks," in *AIAA 2nd Aerospace Sciences Meeting*, New York, NY, 1965.

[24] I. E. Sumner, "Experimentally Determined Pendulum Analogy of Liquid Sloshing in Spherical and Oblate-Spheroidal Tanks," NASA, Washington, D.C., 1965.

[25] J. M. Storey, D. R. Kirk, H. Gutierrez, B. Marsell and P. Schallhorn, "Experimental, Numerical, and Analytical Characterization of Slosh Dynamics Applied to In-Space Propellant Sotrage, Managment,,and Transfer," in *AIAA JPC*, Orlando, FL, 2015.

[26] I. E. Sumner, "Experimental Investigation of Slosh-Suppression Effectiveness of Annular-Ring Baffles in Spherical Tanks," NASA, Washington, D. C., 1964.

[27] I. E. Sumner and A. J. Stofan, "An Experimental Investigation of the Viscous Damping of Liquid Sloshing in Spherical Tanks," NASA, Washington, D.C., 1963.

Appendix

Notes: Some tests were conducted for excitation frequencies and amplitudes not shown in these tables. All tests were repeated once. Water forced excitation tests were only conducted for 20% and 50% volume fraction, and only for 50% with a baffle. Other relevant information can be found in the main body of this thesis.

Damping

Volume Fraction %	Frequency [Hz]	Amplitude [mm]	# cycles 1	# cycles 2
5	1.352	2	5	10
10	1.386	2	6	11
20	1.442	1.5	5	10
30	1.494	1.2	5	10
40	1.549	1	5	10
50	1.628	1	5	10
60	1.685	1	4	5
70	1.778	0.5	6	11
80	1.903	0.5	5	10
90	2.144	0.5	6	10
95	2.405	0.5	5	9

Nonlinear Damping

Volume Fraction %	Frequency [Hz]	Amplitude [mm]	Number of cycles
5	1.352	4	10
10	1.386	4	10

20	1.442	3	10
30	1.494	2.5	8
40	1.549	2	9
50	1.628	1.5	9
60	1.685	1	10
70	1.778	1	9
80	1.903	1	9
90	2.144	1	7
95	2.405	1	6

Damping with a Baffle

Volume Fraction %	Frequency [Hz]	Amplitude [mm]	Number of cycles 1
30	1.494	3	5
40	1.549	3	4
50	1.628	3	5
60	1.685	3	5
70	1.778	3	2
80	1.903	3	1

Forced Excitation

VF %	Frequency [Hz]	A1 [mm]	A2 [mm]	A3 [mm]	A4 [mm]	Number of cycles
20	0.5	10				50
20	1	10				100
20	1.2	10				100
20	1.442	6	1.866	0.934	0.466	100
20	1.6	2				100
20	2	2				150
20	2.48	2				150

20	2.9	2				150
20	3	2				200
20	3.1	2				200
20	3.4	2				200
20	3.5	2				200
20	3.87	2				200
20	4.26	2				250
50	0.5	10				50
50	1	10				100
50	1.5	2				100
50	1.628	6	1.866	0.934	0.466	100
50	1.7	2				100
50	2	2				150
50	2.49	2				150
50	2.8	2				150
50	2.96	2				150
50	3.1	2				200
50	3.4	2				200
50	3.76	2				200
50	4.1	2				250
60	0.5	10				50
60	1	10				100
60	1.5	2				100
60	1.685	6	1.866	0.934	0.466	100
60	1.8	2				100
60	2.2	2				150
60	2.53	2				150
60	2.9	2				150
60	3	2				200
60	3.1	2				200
60	3.44	2				200
60	3.8	2				200
60	4.13	2				250
80	0.5	10				50
80	1	10				100
80	1.5	2				100
80	1.903	6	1.866	0.934	0.466	100
80	2	2				150

80	2.4	2	150
80	2.7	2	150
80	2.9	2	150
80	3.18	2	200
80	3.4	2	200
80	3.67	2	200
80	4	2	250
80	4.36	2	250

Forced Excitation with a Baffle

See “Forced Excitation” table above. No 20% volume fraction tests were conducted with the baffle.